



Synthesis of Nanosize Particles in Thermal Plasmas

65

Yasunori Tanaka

Contents

1	Introduction	2792
2	Fundamentals of Nanoparticle Synthesis by Thermal Plasmas	2792
2.1	Particle Size and Basic Nanoparticle Features	2792
2.2	Dynamics and Evaporation of Feedstock Particles to Atomic Species in Gas Phase	2793
2.3	Thermodynamic Properties	2794
2.4	Gas-to-Particle Conversion: Nucleation, Condensation, and Coagulation	2799
2.5	Particle Growth Due to Coagulation	2802
2.6	General Dynamic Equation for the Discrete Distribution Function	2802
2.7	General Dynamic Equation for the Continuous Distribution Function	2802
2.8	Examples of Modeling Approach for Particle Growth	2803
2.9	Experimental Setups for Nanoparticle Synthesis Using Thermal Plasmas	2805
3	Conclusions	2823
4	Cross-References	2823
	References	2824

Abstract

This chapter is devoted to a description of fundamentals of nanoparticle synthesis using a thermal plasma. Nanoparticles are receiving special attention as the next-generation materials in various industrial fields. To synthesize nanoparticles, thermal plasma is widely used as an effective heat source from its high gas temperature to evaporate feedstock to atomic materials and then as a medium to provide high-temperature gradient field for rapid cooling of evaporated materials.

Y. Tanaka (✉)

Faculty of Electrical and Computer Engineering, Kanazawa University, Kakuma, Kanazawa, Japan
e-mail: tanaka@ec.t.kanazawa-u.ac.jp

Keywords

Nanoparticle · Nanopowder · Thermal plasma · Evaporation of feedstock ·
Nucleation · Coagulation · Condensation

1 Introduction

Nanopowder or nanoparticles are anticipated as promising next-generation elements for use in various applications such as in electronics, energy, and environmental fields because nanoparticles have unique physical and optical properties that differ greatly from the bulk materials. For example, metallic nanoparticles are anticipated as photocatalysts, electrode materials for multilayer capacitance, etc. Oxide and nitride nanoparticles are continually receiving attention for use as photocatalysts (Malato et al. 2007), photonic crystals (Li et al. 2008), photovoltaic cells (Gratzel 2001), gas sensors (Biju and Jain 2008), etc.

Nanoparticle synthesis methods of various types have been developed. Among them, the thermal plasma method is a useful technique to synthesize nanoparticles of various kinds. The thermal plasma has extremely high gas temperatures reaching 10,000 K and simultaneously a high gradient of gas temperature and high gas flow velocity. These characteristics result in rapid evaporation of raw material and then high cooling rates about 10^4 – 10^6 K/s for evaporated materials. This can provide high nanoparticle production rates. Additionally, it can offer nanoparticles in a non-equilibrium or metastable phase because of rapid cooling of materials. In other words, the thermal plasma nanoparticle synthesis is characterized: (1) by a rapid heating through heat transfer from thermal plasma to feedstock and then (2) by a rapid cooling through heat transfer from the vapor material to surrounding gas or wall.

This chapter presents a description of the basics and fundamentals of nanoparticle synthesis using the thermal plasmas. First, the definition of nanoparticles is described briefly. Next, fundamental information related to gas-to-particle conversion is presented briefly with important terms. In addition, two main torches for thermal plasmas are described with their features: direct current (DC) plasma torches and radio-frequency (RF) plasma torches. Finally, a recently developed method to synthesize nanoparticles using a unique technique is introduced: “modulated thermal plasma.”

2 Fundamentals of Nanoparticle Synthesis by Thermal Plasmas

2.1 Particle Size and Basic Nanoparticle Features

Nanoparticles are defined as particles with 1–100 nm diameter. Particles are further classified according to diameter. Previously, the term “ultrafine particles” has been used, which are the same as nanoparticles and of 1–100 nm size. Fine particles

occasionally seem to include particles with sizes of 100–2500 nm. Nanoparticles are receiving great attention as promising elements in various fields such as electronics, catalyst, and also biomedical fields because of their unique characteristics compared to fine particles or bulk materials. Other words are used, such as nanoclusters and nanopowders. Nanoclusters seem to use material particles which have at least one dimension between 1 and 10 nm and a narrow size distribution. Nanopowders are often used as agglomerates or collections of ultrafine particles, nanoparticles, or nanoclusters. Nanometer-sized single crystals, or single-domain ultrafine particles, are often designated as nanocrystals.

Nanoparticles have different properties from those of bulk materials. A bulk material has constant physical properties irrespective of its size. However, nanoparticles have size-dependent properties related to the ratio of the surface area to the particle volume, which is related to the surface effect. Nanoparticles have a larger fraction of atoms at the surface than bulk materials. The unique properties of nanoparticles arise from the large surface area of the material, which dominates the contributions made by the small bulk of the material. Therefore, nanoparticles often have unexpected optical properties. For example, gold nanoparticles are well known to appear red to black in solution. Nanoparticles also have unique thermal properties. Gold nanoparticles have much lower melting temperature around 570 K than that of gold bulk 1300 K. Other size-dependent property changes are quantum confinement in semiconductor particles, surface plasmon resonance in some metal particles, and superparamagnetism in magnetic materials, for example. Consequently, nanoparticles are under the research for application to various fields as promising elements.

2.2 Dynamics and Evaporation of Feedstock Particles to Atomic Species in Gas Phase

Nanoparticle synthesis using thermal plasmas is first characterized by the fact that thermal plasma is used as a high-enthalpy source for feedstock evaporation. Thermal plasmas are well known to have high temperatures about 10,000 K near atmospheric pressure. This offers high enthalpy, which makes it possible to evaporate feedstock in solid or liquid completely. In other words, one can use solid or liquid feedstock with high density compared to gas as a material.

When the feedstock particles are injected into thermal plasmas, the feedstock particle moves from action of the thermal plasma flow as it is heated by the thermal plasma. In this case, there are a momentum transfer and a heat transfer between the feedstock particles and thermal plasmas. The feedstock particles should be not only molten but also be evaporated completely to gas species. This is an important difference from the other applications such as plasma spray coating. After the feedstock particle temperature reaches the evaporation temperature, the feedstock material vapor is created in thermal plasma. That vapor is transported by diffusion and convection in the thermal plasma. The vapor can also change the thermal plasma properties markedly and then the mass, momentum, and energy transfer. This large

change in the thermal plasma properties affects the temperature and gas flow fields in the surrounding thermal plasma. These complex processes have been understood. To consider these complex processes, models based on the PSI-cell (particle source in cell) concept are often used. The PSI-cell concept was developed by Crowe et al. (1977), and it was extended for thermal plasmas by Proulx et al. (1985, 1987). These heat transfer issues from thermal plasmas to feedstock are essentially the same as those in plasma spraying. However, in nanoparticle synthesis, feedstock is often evaporated completely to create atoms or molecules. This makes large affect on the thermal plasma temperature and gas flow fields. Especially, metallic vapor facilitates to change the transport and thermodynamic properties of thermal plasmas markedly, especially electrical conductivity and radiative transfer. These effects should always be considered for thermal plasmas with feedstock injection.

2.3 Thermodynamic Properties

In nanoparticle synthesis process, the feedstock in gas, liquid, or solid phase is injected to high-temperature region in thermal plasmas (Friedlander 2000). The injected feedstock is evaporated to be atoms. Heat transfer between the thermal plasma and injected particles is described in the preceding sections. The evaporated materials in the high-temperature area of the thermal plasma are transported to the downstream portion of the plasma torch. Then they are cooled in the reaction chamber. During the cooling process, the vapor is converted to make nucleation. To elucidate these processes, the basic physics are described here. First, important thermodynamic properties such as saturation vapor pressure, Kelvin relation, etc. will be derived from thermodynamics. Then, the equilibrium size distribution will be mentioned for a basic idea.

2.3.1 Saturation Vapor Pressure and the Supersaturation Ratio

Let us consider a two-phase system for a single component including the vapor A_{vap} and the liquid A_{liq} of the same substance in the equilibrium state $A_{\text{vap}} \rightleftharpoons A_{\text{liq}}$. In this case, if we neglect the effect of surface energy, i.e., assuming a plane surface of the liquid, the following relationship between pressure p and temperature T can be derived under the each equilibrium condition,

$$\frac{dp}{dT} = \frac{\Delta H}{T\Delta v}, \quad (1)$$

where ΔH is the molar heat of vaporization, and Δv stands for the volume change per mole accompanying vaporization of the condensed phase. The volume change can be expressed as $\Delta v = (\bar{v}_{\text{vap}} - \bar{v}_{\text{liq}}) \sim \bar{v}_{\text{vap}}$ because the volume in vapor phase is much greater than that in the liquid phase. In addition, if the vapor depends on the equation of state for an ideal gas, such as $p\bar{v}_{\text{vap}} = RT$ where R is the gas constant, then the following equation can be derived,

$$\frac{dp}{dT} = \frac{\Delta H}{RT^2} p. \quad (2)$$

This equation is well known as the Clapeyron–Clausius equation. This pressure gives the saturation pressure curve $p_s(T)$ as a function of temperature for a plane surface of the liquid without consideration of surface tension effects. If R and ΔH are constants, then $p_s(T)$ is,

$$p_s(T) = p_0 \exp \left[\frac{\Delta H}{R} \left(\frac{1}{T_0} - \frac{1}{T} \right) \right], \quad (3)$$

where p_0 and T_0 , respectively, stand for the reference pressure and the reference temperature. Temperature T_0 is often set to the boiling temperature at atmospheric pressure $p_0 = 101,325$ Pa. This saturation vapor pressure $p_s(T)$ is very important to elucidate the nucleation of nanoparticles.

The ratio of the actual pressure p of the vapor to the equilibrium saturation vapor pressure $p_s(T)$ is called the saturation pressure ratio,

$$S = \frac{p}{p_s(T)}. \quad (4)$$

2.3.2 Kelvin Relation and the Critical Diameter of Nuclei

In this section, a small liquid particle is regarded as the liquid phase material. The surface free energy of the particle is given as $4\pi r^2 \sigma$ where r is the particle radius and σ is the surface tension of the liquid material if the liquid particle is not too small. For the system including the vapor and the particle in liquid, the Gibbs free energy is,

$$G = n_{\text{vap}} \mu_{\text{vap}} + n_{\text{liq}} \mu_{\text{liq}} + 4\pi r^2 \sigma \quad (5)$$

The variation in the free energy dG at constant temperature $dT = 0$ and constant pressure $dp = 0$ can be expressed with the two-phase transition condition $dn_{\text{vap}} = -dn_{\text{liq}}$,

$$dG = \mu_{\text{vap}} dn_{\text{vap}} + \mu_{\text{liq}} dn_{\text{liq}} + d(4\pi r^2 \sigma) \quad (6)$$

$$= dn_{\text{liq}} \left(-\mu_{\text{vap}} + \mu_{\text{liq}} + \left(4\pi \sigma \frac{dr^2}{dn_{\text{liq}}} \right) \right) \quad (7)$$

However, the mole number of the liquid particles n_{liq} can be written,

$$n_{\text{liq}} = \frac{4}{3} \pi r^3 \frac{1}{\bar{v}_{\text{liq}}} \quad (8)$$

Furthermore, the equilibrium condition requires $dG = 0$. Then we obtain,

$$-\mu_{\text{vap}} + \mu_{\text{liq}} + \frac{2\sigma\bar{v}_{\text{liq}}}{r} = 0 \quad (9)$$

This relation expresses the equilibrium between the vapor and the particle in liquid considering the surface tension.

Next, under the equilibrium condition, we can derive a relation between the radius of the particle in the liquid and the pressure at a constant temperature. Differentiating Eq. 9 yields,

$$-d\mu_{\text{vap}} + d\mu_{\text{liq}} + d\left(\frac{2\sigma\bar{v}_{\text{liq}}}{r}\right) = 0 \quad (10)$$

From the Gibbs–Duhem equation with $dT = 0$,

$$(\bar{v}_{\text{vap}} - \bar{v}_{\text{liq}})dp = -2\sigma\bar{v}_{\text{liq}}\frac{dr}{r^2} \quad (11)$$

Using the relation $(\bar{v}_{\text{vap}} - \bar{v}_{\text{liq}}) \sim v_{\text{vap}}$ and the equation of state for vapor $\bar{v}_{\text{vap}} = RT/p$,

$$\frac{RT}{p}dp = -2\sigma\bar{v}_{\text{liq}}\frac{dr}{r^2} \quad (12)$$

Integrating this equation from p_s at $r = \infty$ to $p(r)$ at r with condition $p(r) > p_s$ yields,

$$\ln\frac{p(r)}{p_s} = \frac{2\sigma\bar{v}_{\text{liq}}}{rRT} \quad (13)$$

or

$$p(r) = p_s \exp\left(\frac{2\sigma\bar{v}_{\text{liq}}}{rRT}\right) \quad (14)$$

This expression is well known as the Kelvin relation. The p_s is the saturation vapor pressure for a plane surface $r \rightarrow \infty$. Also, $p(r)$ is the vapor pressure at a radius r of the liquid particle. This result shows that smaller particles have higher vapor pressure.

When the saturation pressure ratio $S = p(r)/p_s (>1)$ is used,

$$d_p^* = 2r^* = \frac{4\sigma\bar{v}_{\text{liq}}}{RT\ln S} = \frac{4\sigma v_l}{k_B T \ln S} \quad (15)$$

In this equation, $v_1 = N_A \bar{v}_{\text{liq}}$ is the volume of monomer in liquid, N_A is the Avogadro number, and k_B denotes Boltzmann's constant ($= R/N_A$). This equation gives the size of nuclei at a certain saturation ratio $S (> 1)$.

2.3.3 Equilibrium Size Distribution

We consider a reaction between a g -class cluster and a $(g-1)$ -class cluster. The reaction $A_{g-1} + A_1 \rightarrow A_g$ happens if condensation occurs by the monomer flux. This reaction rate in unit volume per time is expressed,

$$I_g = \beta s_{g-1} n_{g-1} - \alpha_s s_g n_g \quad (16)$$

Here n_g denotes the density of g -mer, s_g is the surface area of g -mer, and β is the flux of condensing monomers with random thermal velocity,

$$\beta = \frac{1}{4} n_1 v_1 = \frac{1}{4} \frac{p_1}{k_B T} \left(\frac{8k_B T}{\pi m_1} \right)^{\frac{1}{2}} = \frac{p_1}{(2\pi m_1 k_B T)^{\frac{1}{2}}} \quad (17)$$

where m_1 and p_1 , respectively, denote the monomer mass and the pressure. However, α_s is the evaporation flux from g -mer, which is expressed considering a Kelvin relation,

$$\alpha_s = \frac{1}{4} n_s v_1 = \frac{p(r = d_p/2)}{(2\pi m_1 k_B T)^{\frac{1}{2}}} \quad (18)$$

$$= \frac{p_s}{(2\pi m_1 k_B T)^{\frac{1}{2}}} \exp\left(\frac{4\sigma v_1}{d_p k_B T}\right) \quad (19)$$

where $d_p = 2r$ is the g -mer particle diameter in liquid. For this relation, the following relation was used for the diameter of a particle with g and v_1 ,

$$\frac{4}{3} \pi \left(\frac{d_p}{2} \right)^3 = g v_1 \quad (20)$$

For the equilibrium condition $A_{g-1} + A_1 \leftrightarrow A_g$, i.e., the net flux is zero, $I_g = 0$,

$$\beta s_{g-1} n_{g-1} = \alpha_s s_g n_g \quad (21)$$

Substituting Eqs. 17, 19, and 20 into 21, the following relation is obtainable assuming $s_{g-1} \sim s_g$,

$$\frac{n_{g-1}}{n_g} = \frac{\alpha_s}{\beta} = \frac{1}{S} \exp\left[\frac{2\sigma v_1}{k_B T} \left(\frac{4\pi}{3g v_1} \right)^{\frac{1}{3}} \right] \quad (22)$$

Multiplying Eq. 22 varying g from g to 2,

$$\frac{n_{g-1}}{n_g} \frac{n_{g-2}}{n_{g-1}} \dots \frac{n_2}{n_3} \frac{n_1}{n_2} = \frac{n_1}{n_g} = \frac{1}{S^{g-1}} \exp \left[\frac{2\sigma v_1 \left(\frac{4\pi}{3v_1} \right)^{\frac{1}{3}}}{k_B T} \sum_{g=2}^g g^{-\frac{1}{3}} \right] \quad (23)$$

If the g is sufficiently large, then the summation could be the integration,

$$\sum_{g=2}^g g^{-\frac{1}{3}} \sim \int_0^g g^{-\frac{1}{3}} dg = \frac{3}{2} g^{\frac{2}{3}}. \quad (24)$$

Consequently, the equilibrium distribution of nuclei can be expressed,

$$n_g^{\text{eq}} = n_s S^g \exp \left[- \frac{3\sigma v_1 \left(\frac{4\pi}{3v_1} \right)^{\frac{1}{3}} g^{\frac{2}{3}}}{k_B T} \right] \quad (25)$$

Therein, $n_s = p_s/(k_B T)$ and $S = p_1/p_s$. The designation n_g^{eq} is used for n_g obtained for equilibrium state. If the vapor is not saturated, i.e., $S < 1$, then n_g decreases concomitantly with decreasing g . If the vapor is saturated, i.e., $S > 1$, then there is a local minimum at a certain value,

$$g^{\frac{1}{3}} = \frac{2\sigma v_1 \left(\frac{4\pi}{3v_1} \right)^{\frac{1}{3}}}{k_B T \ln S} \quad (26)$$

From this relation and Eq. 20, the critical diameter of nuclei d_p^* is,

$$d_p^* = \frac{4\sigma v_1}{k_B T \ln S}. \quad (27)$$

This critical diameter of nuclei is extremely important to understand the nucleation process in gas-to-particle conversion. In addition, the number density of nuclei with the critical diameter is therefore expressed by,

$$n_g^* = n_1 \exp \left[- \frac{16\pi\sigma^3 v_1^2}{3(k_B T)^3 (\ln S)^2} \right] \quad (28)$$

The number density depends strongly on the saturation ratio S . It is noteworthy that Eq. 25 has a large error for small g . Moreover, the critical number of g^* is,

$$g^* = 36\pi v_1^2 \left(\frac{2\sigma}{3k_B T \ln S} \right)^3. \quad (29)$$

Equation 25 can be rewritten,

$$n_g^{\text{eq}} = n_s S^g \exp\left(-\frac{\sigma s_1}{k_B T} g^{\frac{2}{3}}\right) \quad (30)$$

Therein, s_1 is the surface area of the monomer, n_g^{eq} represents the number density of g -mer in equilibrium state clearly. To obtain this equation, relation $s_1^3 = 36\pi v_1^2$ is used. In addition, Θ signifying the normalized surface tension is,

$$\Theta = \frac{\sigma s_1}{k_B T}. \quad (31)$$

Using Θ , Eq. 30 is rewritten,

$$n_g^{\text{eq}} = n_s S^g \exp\left(-\Theta g^{\frac{2}{3}}\right) \quad (32)$$

2.4 Gas-to-Particle Conversion: Nucleation, Condensation, and Coagulation

In nanoparticle synthesis, using thermal plasmas, the nucleation, condensation, and coagulation occurs to grow nanoparticles. Here, nucleation, condensation, and coagulation will briefly be mentioned (Friedlander 2000).

2.4.1 Homogeneous Nucleation

If condensation occurs, the equilibrium condition is not satisfied. This reaction rate in unit volume per time is again expressed,

$$I_g = \beta s_{g-1} n_{g-1} - \alpha_s s_g n_g \quad (33)$$

According to the homogeneous nucleation theory by Friedlander (2000), the homogeneous nucleation rate I is written,

$$I = 2 \left[\frac{p_1}{(2\pi m_1 k_B T)^{\frac{1}{2}}} \right] \left(n_1 v_1^{\frac{2}{3}} \right) \left(\frac{\sigma v_1^{\frac{2}{3}}}{k_B T} \right)^{\frac{1}{2}} \exp\left(-\frac{16\pi\sigma^3 v_1^2}{3(kT)^3 (\ln S)^2}\right) \quad (34)$$

This can be rewritten using Θ ,

$$I = \beta_{11} n_1^2 \left(\frac{\Theta}{2\pi} \right)^{\frac{1}{2}} \exp\left(-\frac{4\Theta^3}{27(\ln S)^2}\right) \quad (35)$$

To get this equation, we used the relation $\beta s_{g-1} = \beta_{1,g-1} n_1$, where β_{ij} is the collision frequency between i -mer and j -mer. This equation is called classical nucleation theory (CNT) and is widely used to estimate the homogeneous nucleation rate. Furthermore, this homogeneous nucleation rate I was improved by Girshick et al. (1990a) and Girshick and Chiu (1990b) to satisfy monomer and without the constrained equilibrium of the CNT, which can be expressed,

$$I = \beta_{11} n_s^2 S \left(\frac{\Theta}{2\pi} \right)^{\frac{1}{2}} \exp \left(\Theta - \frac{4\Theta^3}{27(\ln S)^2} \right), \quad (36)$$

where S is the supersaturation ratio,

$$S = \frac{p_1}{p_s} = \frac{n_1}{n_s} \quad (37)$$

Subscript 1 and s , respectively, represent the monomer and the saturation state. This equation indicates kinetic nucleation theory and is well adopted to predict the homogeneous nucleation rate for nanoparticle synthesis. The difference between his equation and the CNT is a factor $\exp(\Theta)/S$.

If the particle diameters are much smaller than the mean free path of the vapor, i.e., $d_p \ll \lambda_{\text{vap}}$, then the collision frequency is calculable from the kinetic theory of gases for collisions among rigid sphere particles.

$$\beta_{ij} = \left(\frac{3}{4\pi} \right)^{\frac{1}{6}} \left(\frac{6k_B T}{\rho_p} \right)^{\frac{1}{2}} \left(\frac{1}{v_i} + \frac{1}{v_j} \right)^{\frac{1}{2}} \left(v_i^{\frac{1}{3}} + v_j^{\frac{1}{3}} \right)^2 \quad (38)$$

Therein, ρ_p is the particle density. v_i and v_j , respectively, represent the volumes of particles i and j , which are directly related to the particle diameters. We usually use the relation $v_i = i v_1$, where v_1 is the monomer volume.

Particles are regarded as being produced by homogeneous nucleation in high supersaturation condition. In this case, particles have the critical diameter,

$$d_p^* = \frac{4\sigma v_1}{k_B T (\ln S)} \quad (39)$$

2.4.2 Heterogeneous Condensation

After particle nucleation, condensation can occur to grow the nucleated particle. The condensation occurs on the surface of existing particles if the vapor concentration is high but the supersaturation is not so high. This process is called heterogeneous condensation. This heterogeneous condensation process results in the particle growth without particle density change. Nanoparticles are generally synthesized in the gas phase by homogeneous nucleation and then heterogeneous condensation.

The heterogeneous condensation rate can be estimated from consideration of the exchange of matter and heat between a particle and the surrounding vapor in thermal plasma. We consider a special case in which the mean free path of the vapor is much less than the diameter of the nucleus d_p . For this case, the diffusion equation in spherical coordinates for a single spherical particle under a steady state is expressed,

$$\frac{\partial n(r)}{\partial t} = \frac{1}{r^2} \frac{\partial}{\partial r} \left(r^2 D \frac{\partial n(r)}{\partial r} \right) \quad (40)$$

Therein, $n(r)$ signifies the number density of the surrounding vapor at radial position r ; D is the diffusion coefficient of the vapor. Using the boundary conditions of $n(r \rightarrow \infty) = n_1$ and $n\left(\frac{d_p}{2}\right) = n_d$, we obtain,

$$n(r) = n_1 - \frac{(n_1 - n_d)d_p}{2r} \quad (41)$$

From this solution, the diffusional condensation rate F is given as the following:

$$F = \pi d_p^2 D \left(\frac{\partial n(r)}{\partial r} \right)_{r=d_p/2} \quad (42)$$

$$= 2\pi d_p D (n_1 - n_d) \quad (43)$$

The condensation process can be estimated using the above rate of diffusion condensation flux considering correction from Knudsen number Kn after Fuchs and Sutugin (1964),

$$\frac{dv_p}{dt} = F v_1 \quad (44)$$

$$= 2\pi d_p D (n_1 - n_d) v_1 \frac{1 + Kn}{1 + 1.71 Kn + 1.333 Kn^2}, \quad (45)$$

where v_p signifies the particle volume, v_1 is the molecule volume of condensing species, n_d stands for the number density of vapor at the particle surface, and n_1 represents the density of vapor distant from the particle surface. Density n_d in the saturation state is modified by considering the Kelvin effect, which is especially large for small particles as,

$$n_d = n_s \exp\left(\frac{4\sigma v_1}{d_p k_B T}\right) \quad (46)$$

These simple equations are widely used to predict particle growth for simple situations.

2.5 Particle Growth Due to Coagulation

Further particle growth occurs because of coagulation, which happens by collision between particles. The coagulation results in reduction in the total number of particles and an increase in the particle average size. Presumably, all the particles are spherical; particles i and j collide to form a third particle with volume equal to the sum of the original two particles i and j . Then, the net generation rate of particle k can be described,

$$\left(\frac{dn_k}{dt}\right)_{\text{coag}} = \frac{1}{2} \sum_j \sum_i \beta_{ij} n_i n_j - n_k \sum_i \beta_{ik} n_i. \quad (47)$$

The relation $i + j = k$ should be maintained during summation. Coefficient β_{ij} is the collision frequency between particles i and j , depending on the sizes of the colliding particles and the temperature and pressure. It can include the effects for Brownian coagulation, laminar shear, etc. Eq. 47 is the dynamic equation for the discrete size spectrum changing by coagulation after Smoluchowski (1916).

2.6 General Dynamic Equation for the Discrete Distribution Function

If the convection and diffusion effects are considered, the particle size distribution function (PSDF) is obtained by the following expression,

$$\frac{\partial n_k}{\partial t} + \nabla \cdot (n_k \mathbf{v}) = \nabla \cdot D \nabla n_k + \left(\frac{\partial n_k}{\partial t}\right)_{\text{nucl}} + \left(\frac{\partial n_k}{\partial t}\right)_{\text{cond}} + \left(\frac{\partial n_k}{\partial t}\right)_{\text{coag}} - \nabla \cdot (\mathbf{c} n_k) \quad (48)$$

where D is the diffusion coefficient which is a function of particle size and \mathbf{c} is the particle velocity. Equation 48 is the general dynamic equation for the discrete distribution function where k refers to the number of molecules in the particle. This general dynamic equation (GDE) is also called population balance equation (PDE).

2.7 General Dynamic Equation for the Continuous Distribution Function

When the particle size becomes high ($v \gg v_m$), the discrete distribution can be treated as the continuous distribution for calculation,

$$\begin{aligned} \frac{\partial n(v)}{\partial t} + \nabla \cdot (n(v)\mathbf{v}) &= \nabla \cdot D\nabla n(v) + \left(\frac{\partial n}{\partial t}\right)_{\text{nucl}} - \frac{\partial}{\partial v} (Gn(v)) \\ &+ \frac{1}{2} \int_0^v \beta(\tilde{v}, v - \tilde{v}) n(\tilde{v}) n(v - \tilde{v}) d\tilde{v} \\ &- \int_0^\infty \beta(v, \tilde{v}) n(v) n(\tilde{v}) d\tilde{v} - \nabla \cdot (\mathbf{c}n(v)) \end{aligned} \quad (49)$$

where G is the growth rate due to heterogeneous condensation.

To solve the evolution in time of characteristics of the particles during nucleation process, mainly two approaches are adopted: a discrete-type method like sectional model or nodal model and a method of moments (MOM). The discrete-type method offers more precise and detailed results but requires complicated procedures and high cost for calculation than MOM (Shigeta and Watanabe 2007, 2010). The MOM provides much lower cost calculation for GDE. The method of moments (MOM) solves GDE for low-order moments of the particle size distribution function (PSDF). The k -order moment M_k for $n(v)$ is defined,

$$M_k = \int_0^\infty v^k n(v) dv \quad (50)$$

Using this, Eq. 49 can be written for steady state,

$$\mathbf{u} \cdot \nabla M_k - \left(\frac{\partial M_k}{\partial t}\right)_{\text{nucl}} + \left(\frac{\partial M_k}{\partial t}\right)_{\text{coag}} + \left(\frac{\partial M_k}{\partial t}\right)_{\text{cond}} + \left(\frac{\partial M_k}{\partial t}\right)_{\text{diff}} \quad (51)$$

where $(\partial M_k / \partial t)$ presents net production rate of k -order moments by nucleation, coagulation, condensation, and diffusion. This set of moment equations is unclosed generally by themselves. With assumption of the form of distribution, i.e., the form of log-normal distribution, Eq. 51 can be closed to be solved. There are two main closure methods for nanoparticles: one is the method of moments with interpolative closure (MOMIC) and the other is the quadrature method of moments (QMOM). MOMIC uses interpolation among known whole-order moments to close fractional-order moments due to coagulation and particle surface growth. QMOM was proposed by McGraw (1997), a more precise method than MOMIC. QMOM do not require any assumption of PSDF. It uses a quadrature method to approximate the distribution as a set of weighted particles.

2.8 Examples of Modeling Approach for Particle Growth

Girshick et al. (1988) derived a discrete model to calculate nanoparticle growth as coagulation among clusters and monomers. They calculated particle growth for Fe

and SiC nanoparticles. Girshick and Chiu (1990b) developed a discrete-sectional model by combining their discrete model and the sectional model. This method has been widely used to predict particle growth in different conditions. They successfully predicted MgO nanoparticle growth using the developed model.

The MOM has been well adopted to calculate nanoparticle growth considering nucleation, condensation, and coagulation with combination of thermofluid flow calculation (Proulx and Bilodeau 1989; Girshick et al. 1993; Bilodeau and Proulx 1996; Désilets et al. 1997; Cruz and Munz 1997, 2001; Murphy 2004; Mendoza-Gonzalez et al. 2007a, b; Shigeta and Watanabe 2008). Proulx and Bilodeau (1989) and Girshick et al. (1993) successfully used the MOM to predict Fe nanoparticle growth with thermofluid dynamics for induction thermal plasma synthesis. Bilodeau and Proulx (1996) also obtained two-dimensional thermofluid flow and also particle growth taking into account diffusion, convection, and thermophoresis. Desilets et al. (1997) made a model monomer production from chemical reaction for Si nanoparticles synthesis. Cruz and Munz (1997) used MOM to simulate nucleation and growth of AlN nanoparticles in a transferred arc with Ar/NH₃/H₂ + Al vapor. Titanium nanoparticle formation from Ar–H₂ thermal plasmas with TiCl₄ injection was predicted by Murphy (2004) using MOM. He considered 14 chemical reactions with reaction rates in MOM and studied influence of quench rate. Figure 1 indicates the dependence of titanium yield on quench rate for different initial mixtures of

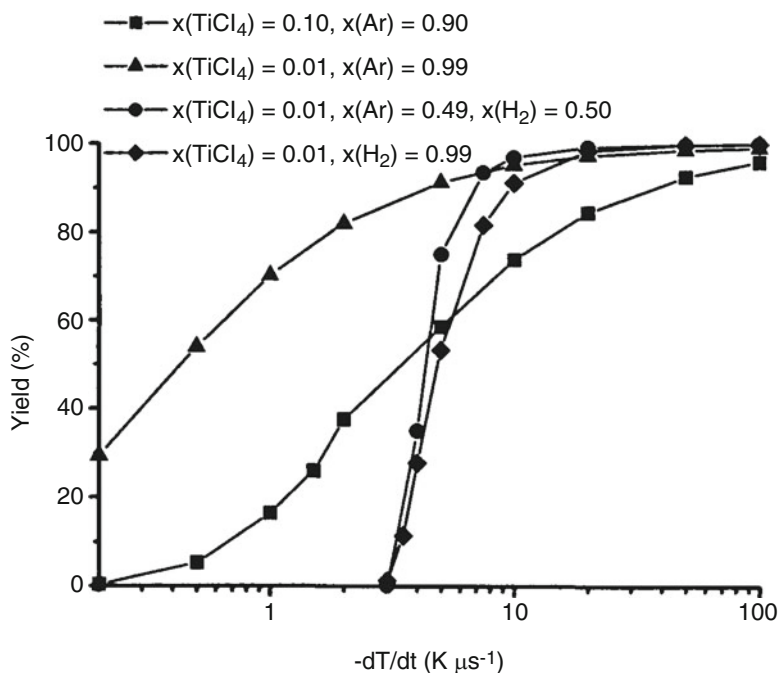


Fig. 1 Dependence of titanium yield on quench rate for different initial mixtures of TiCl₄, Ar, and H₂ (Murphy (2004))

TiCl₄, Ar, and H₂. This calculation was done for high initial temperature to ensure complete dissociation of TiCl₄. It was found from this figure that almost 100% titanium yield could be obtained for sufficiently long residence times at a high temperature and then sufficiently rapid quench rates.

2.9 Experimental Setups for Nanoparticle Synthesis Using Thermal Plasmas

The thermal plasma has a unique feature of high gas temperature above 10,000 K with high power density. This results in a benefit of high enthalpy which facilitates evaporation of injected feedstock into atoms and molecules in gas phase. The evaporated vapor is cooled down by some methods to create nanoparticles. The thermal plasma is thus recognized as an effective heat source for evaporation of the feedstock. In addition, the reactive molecular gas injection into a thermal plasma offers a reactive field. This may provide composite nanoparticles and core-shell structured nanomaterials.

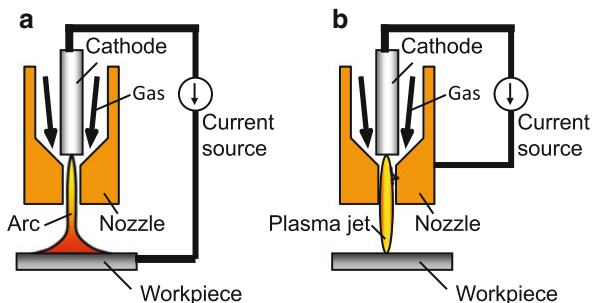
Thermal plasmas of various types such as arc plasmas and inductively coupled thermal plasmas have been adopted for nanoparticle synthesis. Heating mechanism for each of arc plasmas and inductively coupled thermal plasma is so different. Each type of thermal plasmas has a unique feature for thermal plasma field for nanoparticle synthesis. In addition, cooling method for synthesized vapor markedly affects nanoparticle synthesis like size distribution, morphology, composition, phase, etc. Thus, control of heating method and cooling method is essential to control nanoparticle synthesis.

In this section, some results will be introduced for nanoparticle synthesis using thermal plasmas. Nanoparticle synthesis using plasmas including thermal plasmas is well summarized by Fauchais et al. (1997), Ostrikov and Murphy (2007), Shigeta and Murphy (2011), and Seo and Hong (2012). Many researchers have made great efforts to develop some nanoparticle synthesis techniques for these three decades. Nowadays, thermal plasma synthesis is adopted for industrial production of nanoparticles by some companies, for example, Tekna in Canada, Nisshin Seifun in Japan, and Tetronics in the UK, using thermal plasmas. In the following subsection, the basic principles of a DC arc plasma and an RF inductively coupled thermal plasma are briefly introduced. Some examples of nanoparticle syntheses will be described.

2.9.1 DC Arc Plasma Technique

DC arc plasma torches Direct current (DC) arc plasmas are widely used for nanoparticle synthesis. A DC arc plasma is established between the electrodes by DC electric current at several hundred to several thousand amperes. The DC arc plasma is characterized by high gas temperature about 6000–20,000 K, with high gas flow velocity of about 100–1000 m/s at the center axis. The arc voltage reaches ten to several tens of volts. Such high gas temperatures and high gas velocities of arc plasmas are realized especially using arc plasma torches with a gas flow nozzle. Two

Fig. 2 Configurations of (a) transferred arc and (b) non-transferred arc



types of arc plasma torches are usually adopted to form the DC arc plasma for nanoparticle synthesis: the transferred arc plasma torch and the non-transferred arc plasma torch.

Figure 2 presents the configuration of the transferred arc torch and the non-transferred arc torch. Both torches have a gas flow nozzle and a cathode inside the torch. The nozzle is cooled by cooling water inside. This arrangement of the cooled nozzle and the cathode produces strong gas flow to pinch the arc plasma by convection loss. In addition, the arc plasma is further pinched by Lorentz force attributable to the arc current and self-induced magnetic fields. Such pinching phenomena elevate the current density. Then they elevate the arc temperature and arc gas flow velocity. This high temperature and high gas flow velocity are useful for nanoparticle synthesis.

The transferred arc plasma is formed between the cathode inside the plasma torch and the anode outside the plasma torch. In this case, the material to be heated for nanoparticle synthesis is used as the anode. Consequently, just the electrically conductive material is used for the anode corresponding to raw material for nanoparticle synthesis. The anode material is heated by heat transfer from the arc and also by input power to the electrons in electrode fall voltage region. However, the transferred arc plasma is used as an anode. Joule heating occurs only in the arc plasma between the cathode and anode spot. From this arc plasma, the plasma jet is ejected from the nozzle. This plasma jet is used for evaporation of feedstock located outside the torch. In this case, the material by the non-transferred arc plasma or the plasma jet is less efficiently evaporated than by the transferred arc plasma. However, the non-transferred arc presents the important advantage that it can heat electrically nonconductive materials. As other ways, powder feedstock is often used for injection to the plasma jets.

Examples Nanoparticle synthesis has been accomplished at low cost using the transferred arc plasma with high-efficient evaporation of materials. Here, examples are presented of nanoparticle synthesis using a transferred arc and a non-transferred arc.

A transferred arc is often used to produce various types of nanoparticles by many researchers (Uda et al. 1983; Ohno and Uda 1984; Fudoligh et al. 1997; Araya et al. 1988; Watanabe et al. 2001; Lee et al. 2007; Tanaka and Watanabe 2008; Watanabe et al. 2013 etc.). Uda et al. (1983) developed a method to use a transferred arc with

reactive gas like hydrogen to produce metallic nanoparticles. In this method, raw material metal bulk was placed on the anode, which was irradiated by a 50%Ar–50%H₂ transferred arc at atmospheric pressure. The raw metal material is molten by the arc, and then from the molten metal, the metallic nanoparticles were produced. This method uses hydrogen–metal interaction with a high production rate about 0.9 g/min for iron nanoparticles. This rate was found 15 times higher than the simple vaporization method of iron bulk. They also synthesized nitride nanoparticles by a transferred arc with nitrogen gas (Uda et al. 1987). Watanabe et al. (2001) produced Ti nanoparticles using 6 kW Ar–H₂ transferred arc plasmas with a tungsten cathode. In the paper, they mentioned that the H₂ gas inclusion elevates the evaporation rate of Ti bulk anode. The evaporation rate of Ti bulk anode was estimated as 0.2 g/min and found that 5% of the input power was used for the evaporation. Tanaka and Watanabe (2008) also use an Ar–H₂ transferred arc to synthesize Sn–Ag nanoparticles. Figure 3 shows TEM images of Sn–Ag nanoparticles synthesized from 70%Sn–30%Ag ingot. Panel (a) is the result by 100%Ar arc, while panel (b) shows the result by 50%Ar–50%H₂ arc. Nanoparticles synthesized in both conditions have spherical shape. However, the mean diameter was estimated as 19.8 nm and 56.5 nm, respectively, for 100%Ar arc and 50%Ar–50%H₂ arc. This may be due to higher density of metallic vapor arising from higher evaporation rate of the raw material in case of 50%H₂ inclusion. Attention has been paid to carbon nanomaterials from discovery of carbon nanotube by using transferred arcs (Ebbensen and Ajayan 1992; Iijima and Ichihashi 1993; Ando et al. 2000; Shi et al. 2000; Kim et al. 2006, 2007, 2009, 2017). Ando et al. (2000) developed a mass production method for single-wall carbon nanotube (SWCNT) with a production rate of 1.24 mg/min by using a DC arc plasma with two graphite electrodes (Figs. 4 and 5) (Ando et al. (2000)). The AlN nanoparticles were synthesized by a transferred arc in Cruz and Munz (1997). They separated a reaction section from the plasma reactor, and the Al vapor is generated by

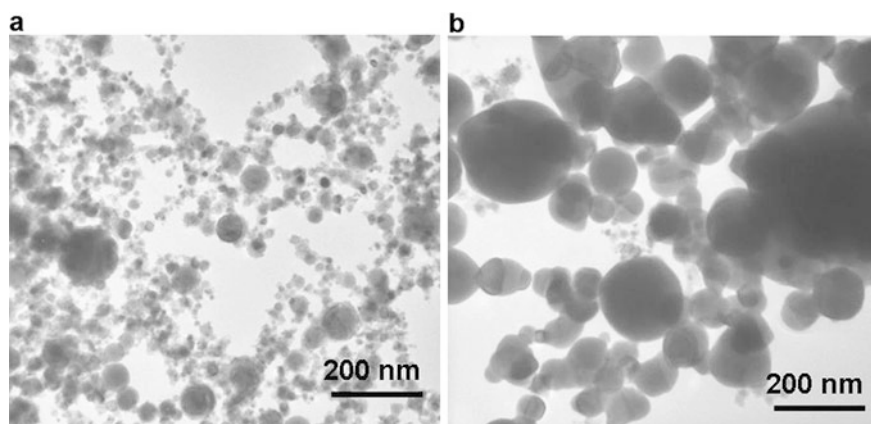
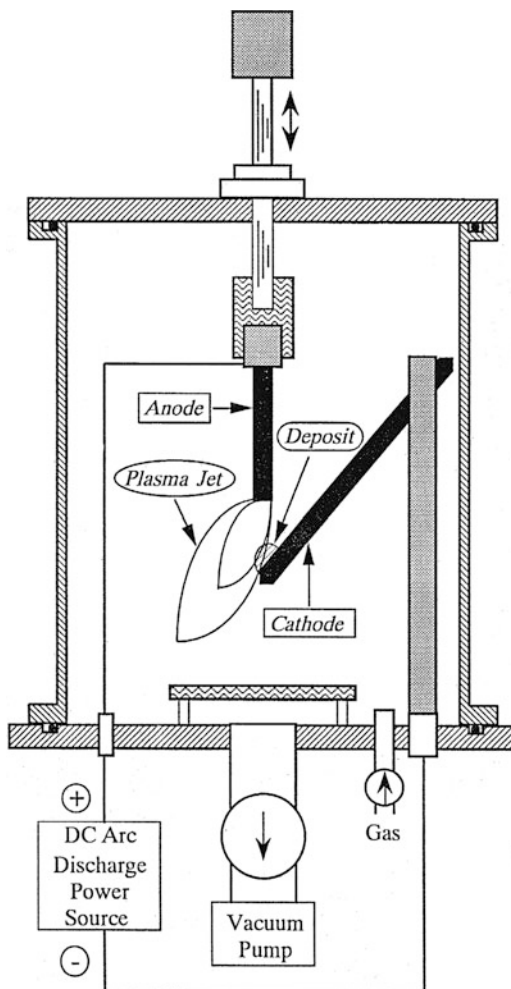


Fig. 3 TEM images of nanoparticles prepared from 30wt%Ar–70%Sn ingot raw material. (a) 100%Ar arc, (b) 50%Ar–50%H₂ (Tanaka and Watanabe 2008)

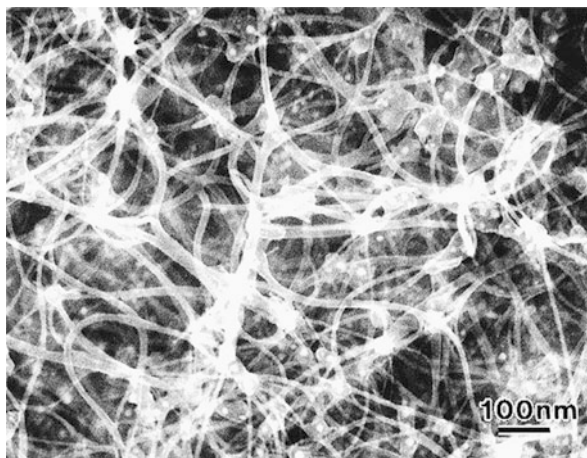
Fig. 4 A schematic diagram of the DC arc plasma jet (APJ) apparatus (Ando et al. 2000)



the transferred arc, and it was mixed with Ar/NH₃ gas to synthesize AlN nanoparticles. For this method, they also developed a numerical model for nucleation and particle growth.

Cubic boron nitride nanoparticles are now also receiving attention because of their high hardness and high thermal conductivity. Recent example of nanoparticle synthesis using transferred arc are as follows: Ko et al. (2015) synthesized cubic boron nitride nanoparticles by a transferred Ar–N₂ thermal plasma at 13.5 kW at atmospheric pressure. They used boron oxide (B₂O₃), melamine (C₃H₆N₆), and NH₃ as raw materials. Then, they synthesized c-BN nanoparticles with sizes smaller than 150 nm. Stein and Kruijs reported optimal process conditions for a single transferred arc electrode pair for pure metal nanoparticle synthesis with a high production rate (Stein and Kruijs 2015, 2016). They also have done a scaled-up approach with

Fig. 5 A characteristic SEM image of cottonlike carbon soot produced by APJ method (60A, He 500 torr) (Ando et al. 2000)



parallelization of multiple transferred arcs and synthesized copper nanoparticles with mean size of 79 nm with a production rate of 69 g/h. Kulkarni et al. (2009) reported nanoparticle synthesis of Al_2O_3 , AlN , and Fe_xO_y , using a DC transferred arc plasma, indicating the effect of pressure on their crystalline phases.

Non-transferred arcs are also used for nanoparticle synthesis (Oh and Park 1998; Tong and Reddy 2005, 2006). One feature of the non-transferred arc involves raw material injection to arc jet to evaporate it. Another feature of this method is a less erosion of electrodes compared to transferred arcs. Choi et al. (2006) developed a continuous production method of classical nucleation theory using non-transferred arc jet with methane. Figure 6 indicates a developed arc jet plasma reactor for CNT synthesis by decomposition of CH_4 . The cathode was made of tungsten, and a copper nozzle is used as an anode. Catalyst Ni and Y powder was directly injected into arc plasma jet. They successfully synthesized CNTs in continuous mode. They found multiwalled CNTs which were mainly produced in high purity with a few other structures of nanotubes observed. Similar continuous synthesis method has been reported by Bystrzejewski et al. (2008). On the other hand, Kim et al. prepared AlN nanoparticles using non-transferred arc (Kim et al. 2013). A pellet of micro-sized aluminum (Al) powders was evaporated using an argon–nitrogen thermal plasma flame. Also, ammonia (NH_3) was introduced into the reactor as a reactive gas. They studied effect of NH_3 gas flow rate on the size and the crystallinity of the synthesized AlN particles. Supersonic thermal plasma expansion has been used for nanoparticle synthesis (Goortani et al. 2006; Kakati et al. 2008; Bora et al. 2010, 2012, 2013). Bora et al. (2013) studied synthesis of nanostructured TiN using a supersonic thermal plasma expansion. Figure 7 shows the reactor configuration for nanoparticle synthesis using thermal plasma expansion process. The supersonic thermal plasma can avoid problems of broad particle size distribution and serious interparticle agglomeration that conventional thermal plasmas have encountered. The supersonic thermal plasma expansion provides narrower size distribution because of less agglomeration due to the directed supersonic velocity of the particles

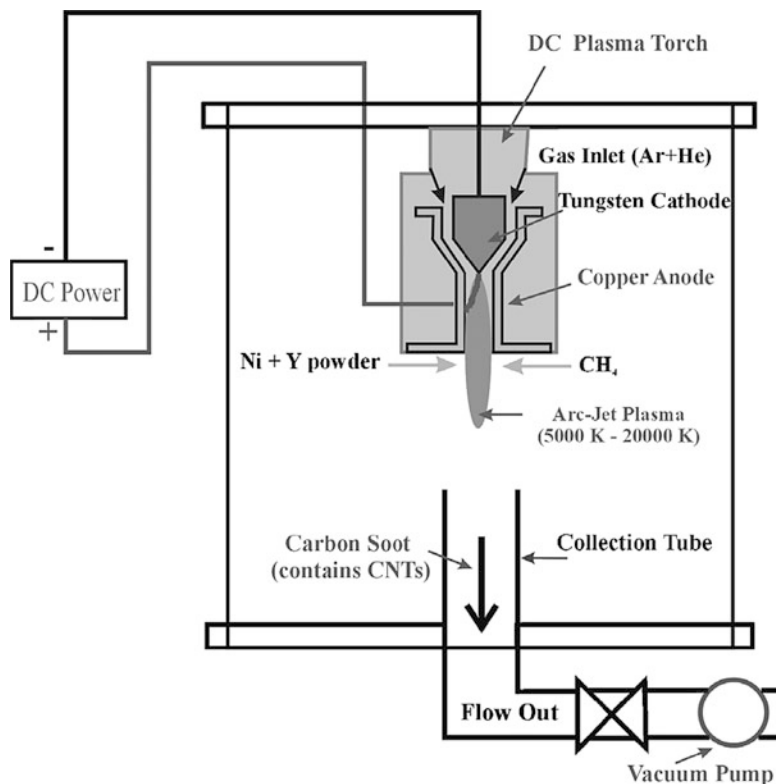


Fig. 6 Schematic diagram of an arc jet plasma reactor for CNT synthesis by decomposition of CH_4 (Choi et al. 2006)

embedded in the plasma. They successfully synthesized mono-crystalline TiN nanoparticles with mean diameter of 15 nm from TiCl_4 and NH_3 as reactants.

2.9.2 Radio-Frequency (RF) Inductively Coupled Thermal Plasma Technique

Principle of RF inductively coupled thermal plasma Inductively coupled thermal plasma (ICTP) or induction thermal plasma (ITP) is established by electromagnetic coupling without electrode. Because there is no electrode, the thermal plasma is almost entirely uncontaminated by impurities. This lack of contamination from the electrodes is extremely useful to synthesize pure nanoparticles.

Figure 8 shows the typical RF ICTP torch configuration. The RF ICTP torch is usually composed of a dielectric cylindrical tube and the coil surrounding the tube. To this coil, the radio-frequency coil current is supplied to generate an alternative magnetic field in axial direction and alternative electric field in the azimuthal direction. This electric field can accelerate an electron present in the torch. Then the accelerated electron collides with the gas species. If the kinetic energy exceeds

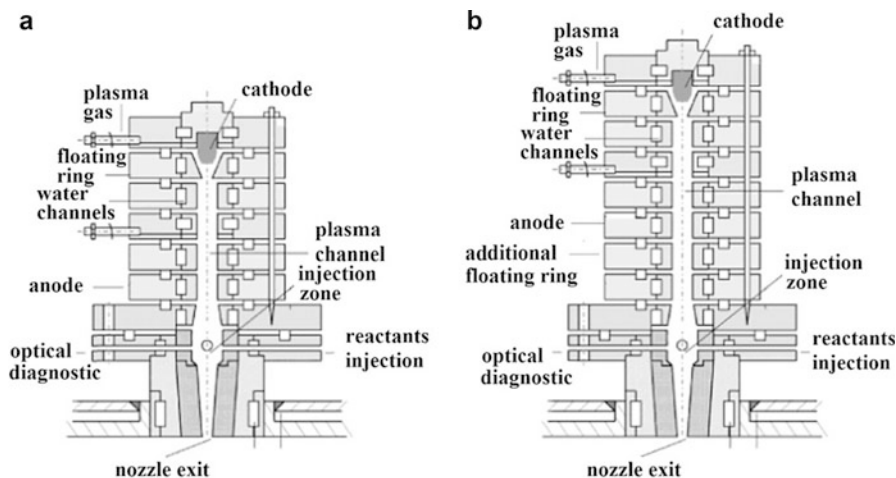
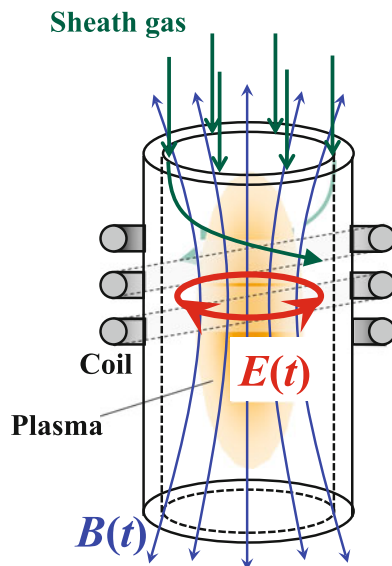


Fig. 7 Reactor configurations for injection of reactants (a) at the hot zone just after the anode and (b) at the colder tail zone of the plasma flame, where the torch has two additional floating rings after the anode (Bora et al. 2013)

Fig. 8 Configurations of radio-frequency inductively coupled thermal plasma



the ionization potential of gas species, then the gas is ionized to produce the thermal plasma inside the torch. Some feedstock in solid powder, liquid, or solution and suspension is used for nanoparticle synthesis. The feedstock is injected from the head of the torch. Usually, a water-cooled powder feeding probe is inserted into the

thermal plasma to avoid feeding powder in backflow there. The injected feedstock is heated by the thermal plasma to increase the feedstock temperature. This increase in the temperature results in melting and evaporation of the feedstock.

The important benefits of the ICTP are that it is (1) free from contamination, (2) with a large diameter thermal plasma with high gas temperature, and (3) with slow gas flow velocity of several tens of meters per second compared to a DC arc plasma and a plasma jet. This slow gas flow velocity results in long residence time of the feedstock. Long residence time of the order of 10 ms supports sufficient evaporation of the feedstock and also sufficient reactions. Another benefit is that any reactive gas is useful for chemical reaction without concern related to electrode erosion. However, molecular gas injection involves dissociation in thermal plasma, which takes power from the thermal plasma. In addition, as well known, Yoshida et al. (1983) developed a unique plasma torch: the hybrid plasma torch in which an RF inductively coupled thermal plasma with a DC arc plasma jet (Fig. 9). This technique is greatly useful to the stable operation of an RF induction thermal plasma with injection of feedstock and efficient heating of the particles around the center axis of the torch with wider high-temperature area. The hybrid plasma torch has been widely used for nanoparticle synthesis as well as plasma spraying.

Examples The ICTP is widely used to synthesize nanoparticles of various kinds such as metallic, oxide, nitride, carbide, and other compounds because of the advantages of ICTP.

Nanoparticle synthesis using an RF induction thermal plasmas has continuously been developed from pioneering works (Yoshida et al. 1979; Guo et al. 1995). Following the works, many researchers used radio-frequency (RF) inductively coupled thermal plasma torch to synthesize various kinds of nanoparticles: nitrides (Yoshida et al. 1979; Lee et al. 1990; Soucy et al. 1995; Cruz and Munz 2001, etc.), carbides (Eguchi et al. 1989; Guo et al. 1995; Gitzhofer 1996; Leparoux et al. 2005; Ishigaki et al. 2005; Thompson et al. 2013, etc.), oxides (Oh and Ishigaki 2004; Goortani et al. 2006; Li et al. 2007; Ishigaki and Li 2007; Marion et al. 2007; Zhang et al. 2014, etc.), and some metals (Yoshida and Akashi 1981; Harada et al. 1985; Anekawa et al. 1985; Son et al. 2002; Boulos et al. 2006; Cheng et al. 2014; Tanaka et al. 2016; Sone et al. 2016, etc.). Doped nanoparticles, intermetallic nanoparticles, and core-shell nanoparticles are also synthesized using inductively coupled thermal plasmas.

Yoshida et al. (1979), Guo et al. (1995), and Gitzhofer (1996) contributed syntheses of SiC nanoparticles or ultrafine powders using an induction thermal plasma at a high power above 40 kW. They investigated experimentally feedstock size and feeding probe position on the evaporation rate of Si feedstock and then numerically studied heat and mass transfer in the RF induction thermal plasma with reactive gas CH₄. These results have become a base of nanoparticle synthesis using RF induction thermal plasmas.

Ishigaki and Li (2007) investigated cooling effect of thermal plasma by injection of quenching gas for nanoparticle synthesis. The cooling of the vapor and gas is essential for high efficiency and control of nanoparticle synthesis. It also influences the composition of synthesized nanoparticles. Figure 10 indicates experimental

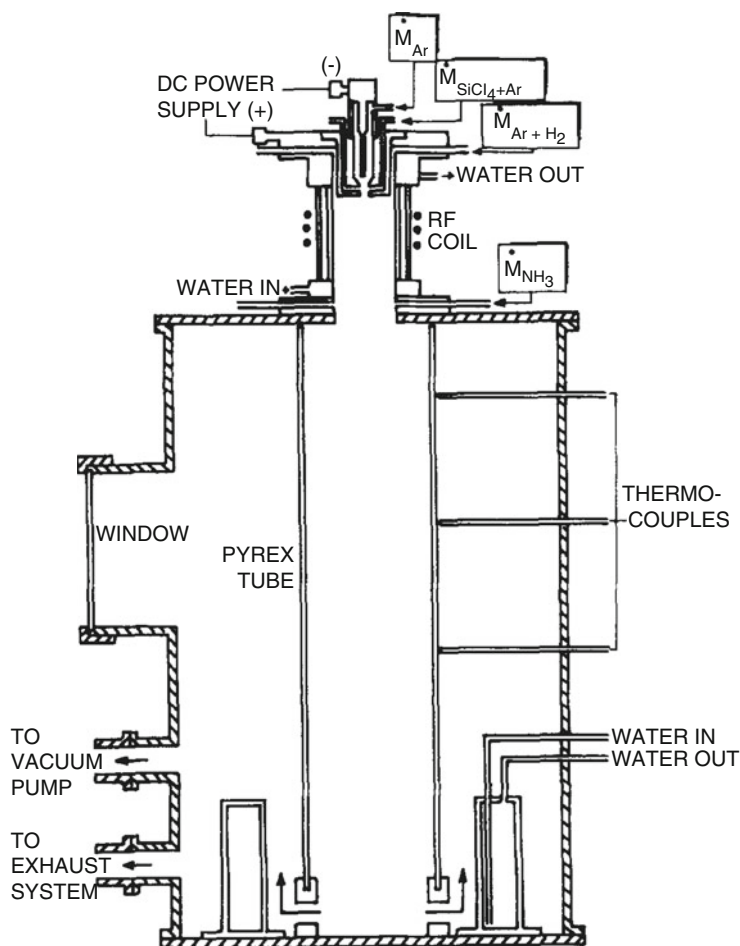


Fig. 9 Schematic view of a hybrid plasma reactor chamber designed for the preparation of ultrafine Si_3N_4 (Yoshida et al. 1983)

setups with different quenching gas directions: (a) transverse swirl-flow injection and (b) counterflow injection. The direction of the quenching gas injection influences cooling effect of vapors. Figure 11 shows the calculated streamlines and temperatures for Ar quenching gas injection with the above directions. The predicted trajectories of a test particle are also presented. The Ar/O₂ RF induction thermal plasma is assumed for TiO₂ nanoparticle synthesis, and liquid precursor was adopted. Titanium dioxide has high photocatalyst ability for UV light, and it is used for photocatalyst, photonic crystal, photo-electrochemical cells, and various sensors. As seen, when Ar quenching gas is injected counter to the plasma plume, the temperature field and also the trajectories of the particle are profoundly affected. The authors found that a test particle experiences high-temperature zone in a shorter

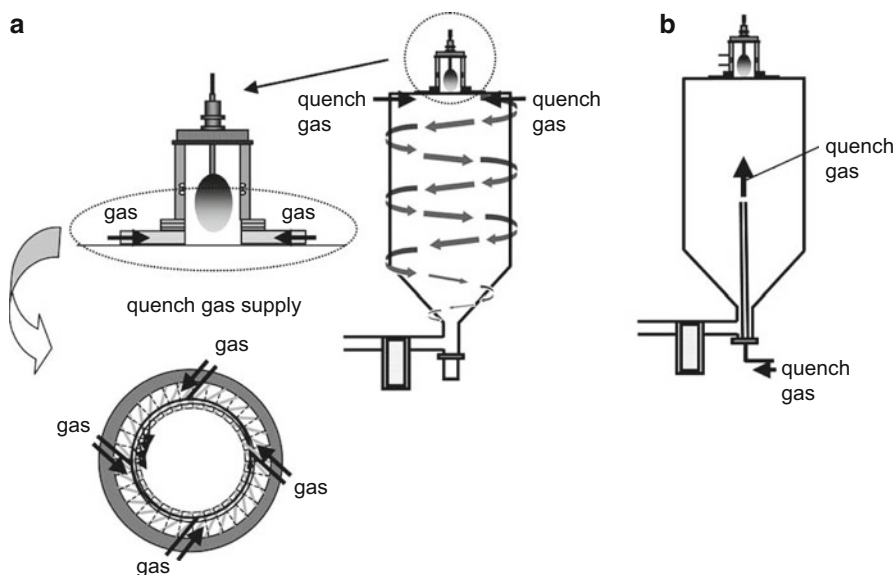


Fig. 10 Experimental setups for transverse swirl-flow injection (a) and counterflow injection (b) of quench gases (Ishigaki and Li 2007)

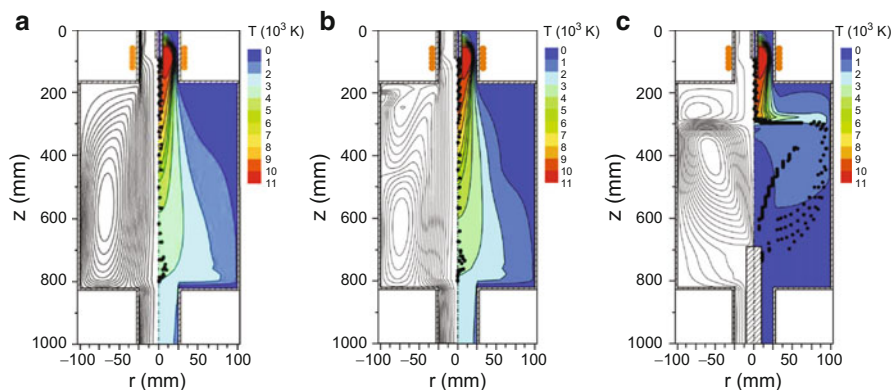


Fig. 11 Streamlines and temperature distribution for (a) no quench gas, (b) transverse swirl-flow injection of Ar at 100 slpm, and (c) counterflow injection of Ar at 100 slpm (Ishigaki and Li 2007)

duration and that it favors the formation of finer particles. They also investigated synthesis of phase-controlled TiO_2 nanoparticles (Li and Ishigaki 2004) and the synthesis of metallic ion-doped TiO_2 nanoparticles using an RF induction thermal plasma (Wang et al. 2005; Zhang et al. 2010, 2014). Metallic ion-doped TiO_2 nanoparticles like Eu^{3+} -doped TiO_2 , Fe^{3+} -doped TiO_2 , and Eu^{3+} - Nb^{5+} -co-doped TiO_2 were successfully synthesized using the RF induction thermal plasmas. The

impurity doping markedly improves photocatalyst efficiency for visible light (Barolo et al. 2012).

Metallic nanoparticles have been synthesized using an RF inductively coupled thermal plasmas. Kim et al. reported synthesis of nickel nanoparticles using inductively coupled thermal plasma with a $\text{Ni}(\text{OH})_2$ micro-powder feedstock (Kim et al. 2016). Nickel nanoparticles are intended for use as internal electrodes of multilayer ceramic capacitors (MLCC). They studied the dependence of process parameters on the size and morphology of synthesized nanoparticles. They also synthesized core-shell structured composite powders using induction thermal plasmas (Kim et al. 2017). Recently, attention is paid to nanomaterials for energy issue solution. One of them is nanomaterials for electrical batteries. Si nanoparticles are promising elements which can be used for anode material in lithium ion batteries (LIB). Reaction chamber geometries for Si nanoparticle synthesis with an RF thermal plasma were studied by numerical thermofluid simulation by Colombo et al. (2012, 2013). They also investigated gas injection along the wall and found the advantage of the conical chamber geometry on the high yield of nanoparticles.

Tanaka et al. (2016) and Sone et al. (2016) reported synthesis of lithium metal oxide composite nanoparticles by induction thermal plasmas. Lithium metal oxide composite nanoparticles are expected as cathode materials for solid oxide fuel cell. They synthesized Li-metal oxide nanoparticles of various shapes in Li-Mn, Li-Cr, Li-Ni, and Li-Co systems with Ar/O_2 induction thermal plasma. They used solid mixture powder feedstock of Li_2CO_3 and MnO_2 . Figure 12 shows an SEM image of the as-prepared nanoparticles. As seen, synthesized LiMnO_2 has a tetradecahedral crystalline structure. They found that such spinel-structured LiMn_2O_4 nanoparticles were successfully obtained by controlling the admixture ratio of O_2 to Ar in the thermal plasma. They also studied the formation mechanism of Li-Mn oxide nanoparticles theoretically. They found that in the Li-Mn oxide nucleation system, MnO nucleation is first initiated, and then MnO and Li_2O vapors co-condense on the formed nucleus, then forming LiMn_2O_4 .

Fig. 12 Representative SEM image of the LiMn_2O_4 nanoparticles prepared under an O_2 flow rate of 2.5 L= min. The powder feed and carrier gas flow rates used in this experiment are 0.4 g=min and 3 L=min, respectively (Sone et al. 2016)

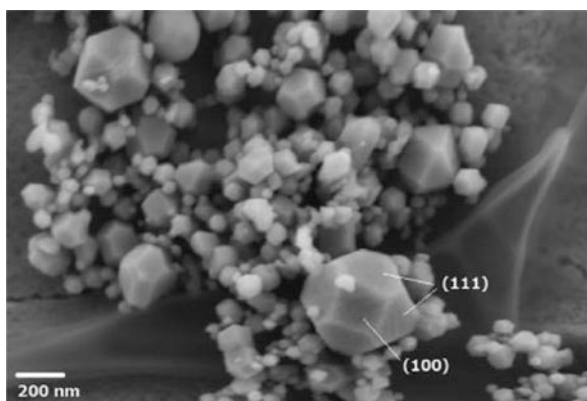
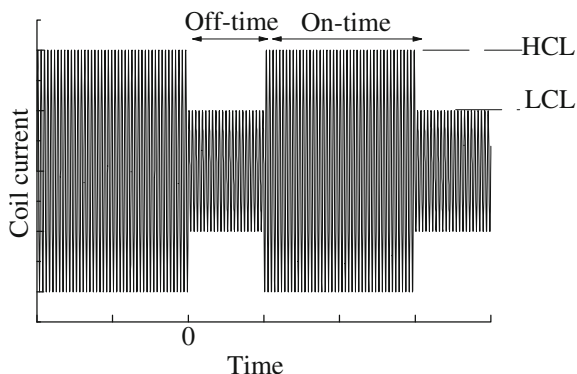


Fig. 13 Modulated coil current and modulation parameter definitions (Kodama et al. 2014)



2.9.3 New Technology: Modulated Induction Thermal Plasmas

Methodology of a large-scale nanopowder synthesis system Recently, a unique method for nanoparticle synthesis at a high production rate was developed by Tanaka et al. (2010, 2012): the PMITP–TCFF method. The PMITP is the pulse-modulated induction thermal plasma. The TCFF is time-controlled feeding of feedstock. Here, details of the developed method are introduced for synthesis of large amounts of Al³⁺-doped TiO₂ nanopowders (Kodama et al. 2014).

The developed PMITP–TCFF method uses the pulse-modulated induction thermal plasma (PMITP), which is sustained with the coil current of approximately several hundred amperes, the amplitude of which is modulated into a rectangular waveform (Kodama et al. (2014)). Such modulation of the coil current can repetitively produce a high-temperature field during the “on-time” and a low-temperature field during “off-time” in thermal plasmas. Figure 13 portrays the coil current modulated into a rectangular waveform along with the definition of modulation parameters. As presented in Fig. 13, the on-time is the time period with the higher current level (HCL); although the off-time is the time period with the lower current level (LCL). We have also defined a shimmer current level (SCL) as a ratio of LCL to HCL. The duty factor (DF) has also been defined as the ratio of on-time in one modulation period. A condition of 100%SCL or 100%DF corresponds to the non-modulation condition. A lower SCL condition is equivalent to a condition with a larger modulation degree.

Figure 14 presents the methodology developed for the synthesis of large amounts of nanopowder using the PMITP–TCFF method. The PMITP can repetitively produce a higher temperature field and a lower temperature field according to the coil current modulation. To this PMITP, the feedstock solid powder is supplied through a powder feeding tube from a powder feeder along with Ar carrier gas from the top of the plasma torch head to the PMITP. Furthermore, a high-speed valve is installed on the tube between the powder feeder and the plasma torch. Setting the open and close timing of the valve can control the actual timing and the time length of the powder feeding.

The right-hand side of Fig. 14 shows a timing chart of the coil current modulation, switching signal of the solenoid valve, and actual powder feeding. For synthesis of

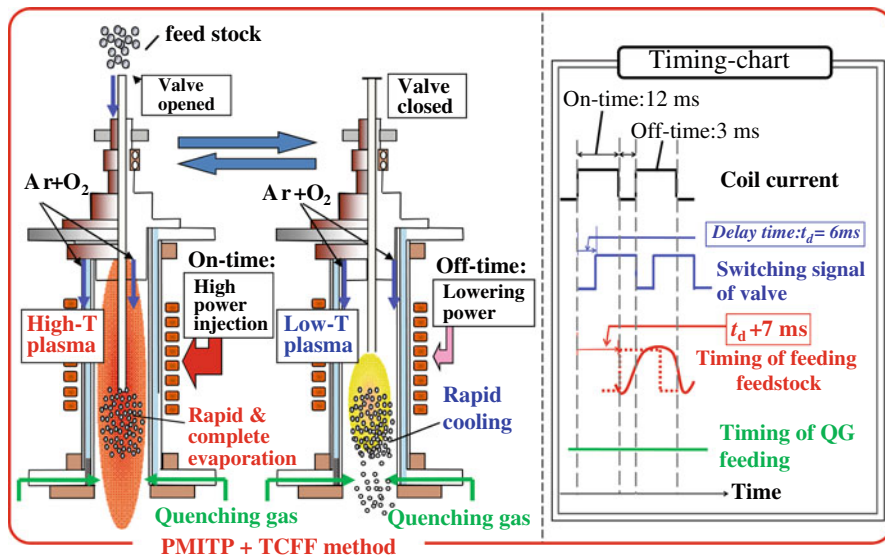


Fig. 14 Method for large-scale nanopowder synthesis using pulse-modulated induction thermal plasma with time-controlled feedstock feeding (PMITP–TCFF) (Kodama et al. 2014)

large amounts of nanopowder, heavy-load feeding of feedstock is necessary without extinction of the plasma or incomplete evaporation of the feedstock. In the developed PMITP–TCFF method, the feedstock powder is controlled to be fed intermittently and synchronously only during the high-temperature period in the on-time of the PMITP. This synchronized powder feeding can be executed easily by controlling the delay time t_d for the opening timing of the valve in reference to the pulse modulation signal of the PMITP.

The injected feedstock powder with heavy load is evaporated rapidly, completely, and efficiently in high-temperature plasma during the on-time of the PMITP because of higher power injection to the PMITP. The feedstock injection is stopped by closing the solenoid valve during the successive off-time. During the off-time, the evaporated feedstock material is cooled rapidly because the thermal plasma temperature decreases as a result of the decreased input power to the PMITP. This rapid cooling might promote particle nucleation from evaporated atomic materials in vapor in the PMITP. Nucleated particles are transported downstream of the PMITP torch with particle growth. Downstream of the PMITP torch, the quenching gas is injected in the radial direction. Such a quenching gas injection cools the evaporated material further to restrain the synthesized particle growth. Then, in the successive on-time, the input power increases to rebuild high-temperature thermal plasma for the subsequent powder injection. In this way, the PMITP–TCFF method described above can create effective vaporization of the feedstock and support effective cooling of the evaporated material. It enables synthesis of large amounts of nanopowder.

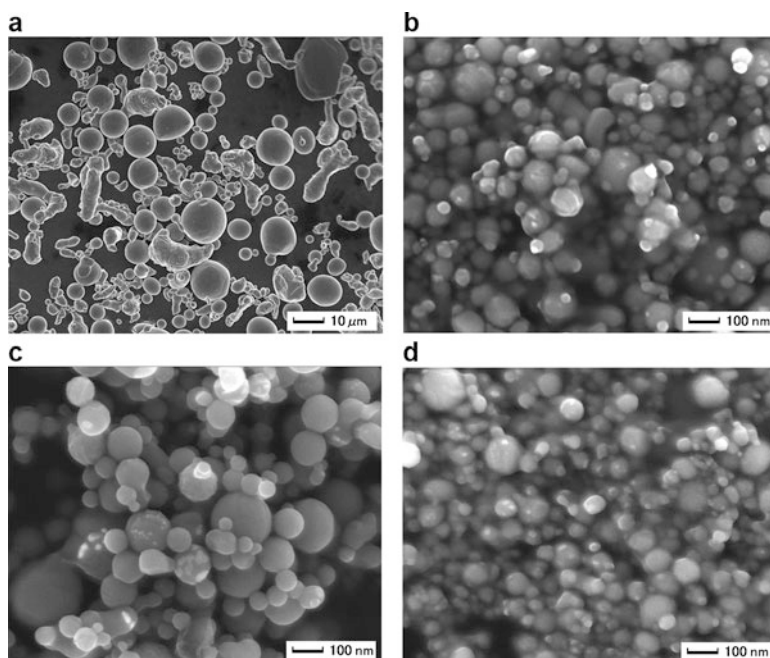


Fig. 15 FE-SEM images for (a) feedstock and synthesized powder with conditions (b) 80%SCL, $g_{\text{pow}} = 12 \text{ g min}^{-1}$, (c) 70%SCL, $g_{\text{pow}} = 12 \text{ g min}^{-1}$, and (d) 60%SCL, $g_{\text{pow}} = 19 \text{ g min}^{-1}$ (Kodama et al. 2014)

Results and discussions Figure 15 presents FE-SEM images of feedstocks and the synthesized nanopowder collected at the filter under different SCL conditions (Kodama et al. 2014). The averaged input power and the pressure were 20 kW and 300 torr, respectively, and 95wt%Ti-5%Al was used. The feedstock Ti powder has mean diameter of approximately $27 \mu\text{m}$ with various shapes. However, most synthesized particles were found to have size of 100 nm or less in any of the three SCL conditions in the present experiments. Therefore, nano-sized particles were produced despite heavy-load feeding of the feedstock using our developed method. The synthesized particle shapes were observed to be almost spherical for these three conditions, which implies that nanoparticles were synthesized and grown in gas phase rather than on the filter or wall surface. It was also found that the mean particle diameter can be controlled by SCL. Based on these results and weight measurements of the synthesized powder, the production rates of nanopowder were estimated as higher than 400 g h^{-1} using the 20-kW PMITP. This production rate value is 10–20 times higher than those obtained using the conventional thermal plasma method reported in the literature (Tsai et al. 2012; Lee et al. 2004).

Figure 16 presents BF-TEM images and TEM/EDX mapping results of synthesized nanopowder collected at the filter. Panel (a) presents results for the condition of 80%SCL with a powder feed range g_{pow} of 12 g min^{-1} , whereas panel (b) shows

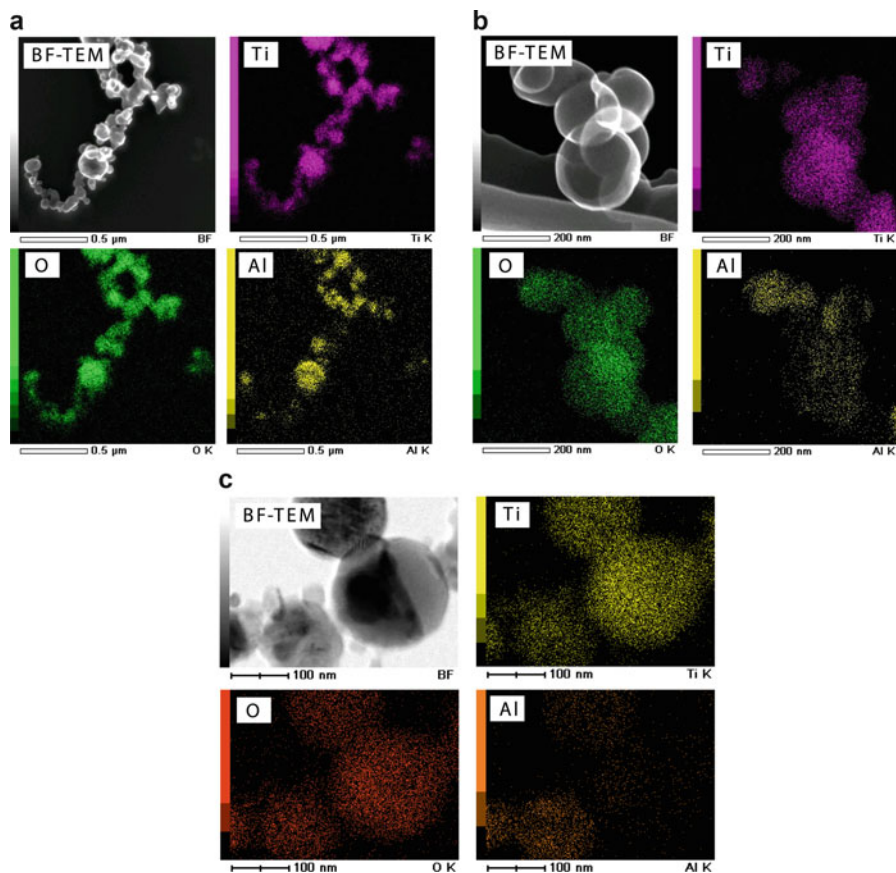


Fig. 16 BF-TEM and TEM/EDX mapping for (a) 80%SCL, $g_{\text{pow}} = 12 \text{ g min}^{-1}$, (b) 70%SCL, $g_{\text{pow}} = 12 \text{ g min}^{-1}$, and (c) 60%SCL, $g_{\text{pow}} = 19 \text{ g min}^{-1}$ (Kodama et al. 2014)

results for the condition 70%SCL and $g_{\text{pow}} = 12 \text{ g min}^{-1}$. Finally, panel (c) shows the results for the condition 60%SCL and $g_{\text{pow}} = 19 \text{ g min}^{-1}$. Each panel has a BF-TEM image and Ti, O, and Al element distributions. Magnifications of TEM images and TEM/EDX mapping differ among panels. From the BF-TEM images, results show that spherical nanoparticles without mesopores were synthesized for these three SCL conditions. The TEM/EDX mapping shows that Al was detectable and that it was distributed almost uniformly in the synthesized particles similarly to Ti and O for 80%SCL and 70%SCL. That result, considered together results of XRD and XPS analysis, as described later, means that elemental Al might be distributed almost uniformly on the synthesized TiO_2 nanoparticles by our developed PMITP-TCFF method with heavy-load feeding of feedstock. After other analyses using XRD, XPS, and optical property measurements, the synthesized nanoparticles were found to be Al^{3+} -doped TiO_2 .

In this way, results showed that the PMITP–TCFF method can synthesize Al^{3+} -doped TiO_2 nanopowder in large amounts. Effects of the coil current modulation degree are found to offer a high evaporation rate and efficient nucleation of nanoparticles, with the control of the mean particle diameter synthesized. The final production rate was estimated as higher than 400 g h^{-1} .

Spectroscopic observation of feedstock evaporation and precursor formation A key point to enhancing production efficiency is to elucidate nanoparticle formation mechanisms in an induction thermal plasma torch. Recently, Tanaka et al. have investigated the mechanism using a two-dimensional spectroscopic observation technique during TiO_2 NP synthesis. Results show that the two-dimensional spectroscopic observation system can produce temporal variation of two-dimensional radiation intensity distributions of Ti I and TiO spectra in the PMITP (Kodama et al. 2016).

The intermittent injection of the feedstock was conducted using a high-speed solenoid valve. The open (t_{open})/close time (t_{close}) of the solenoid valve was regulated at 8/22 ms (27%DF_{valve}). This condition corresponds to an almost single-shot feeding of feedstock, which can avoid interaction between single powder feedings during intermittent feeding.

Figure 17a again shows the observation result of Ti I intensity variation for a valve opening time t_{open} of 8 ms; Fig. 17b is the observation result of TiO intensity variation for t_{open} of 8 ms. These were observed simultaneously using the two-dimensional spectroscopic imaging system. However, Fig. 17c–e, respectively,

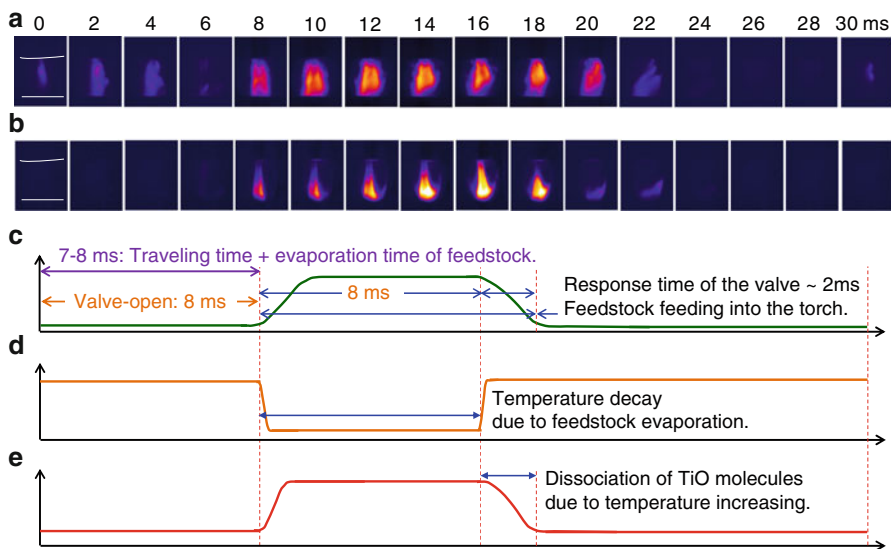


Fig. 17 Understanding of Ti feedstock evaporation and precursor TiO molecules in the torch: (a) Observation result for Ti I in valve open condition of 8 ms; (b) observation result for TiO in valve open condition of 8 ms; (c) estimated timing of feedstock injection into the torch; (d) estimated temporal variation of temperature; and (e) estimated timing of formation of precursor TiO molecules (Kodama et al. 2016)

show our estimated time chart showing Ti feedstock injection into the torch, the temperature variation in the torch, and the temporal variation in formation of precursor TiO molecules. In addition, Fig. 18 shows the physical picture with comments inferred for the temporal and spatial distribution of Ti atomic density and TiO molecular density in the case of 20%DF_{valve}. In this figure, the green region shows the distribution of dense Ti atom; the red region shows the distribution of dense TiO molecule. Figure 18a is the inferred temperature distribution before injection of Ti feedstock into the torch. Figure 18b shows the introduction of Ti feedstock to the torch, Ti evaporation, and initiation of TiO formation at $t \sim 7$ ms. Figure 18c depicts the mixing of Ti and O atoms and formation of TiO at $t \sim 14$ ms. Figure 18d shows the transport of TiO to the downstream of the torch at $t \sim 18$ ms. Figure 18e presents the decrease in TiO density and increase in Ti atomic density attributable to dissociation reaction of $\text{TiO} \rightarrow \text{Ti} + \text{O}$ by temperature recovery at $t \sim 20$ ms. Figure 18f shows the decrease in Ti density attributable to convective transport to the downstream of the torch at $t \sim 22$ ms.

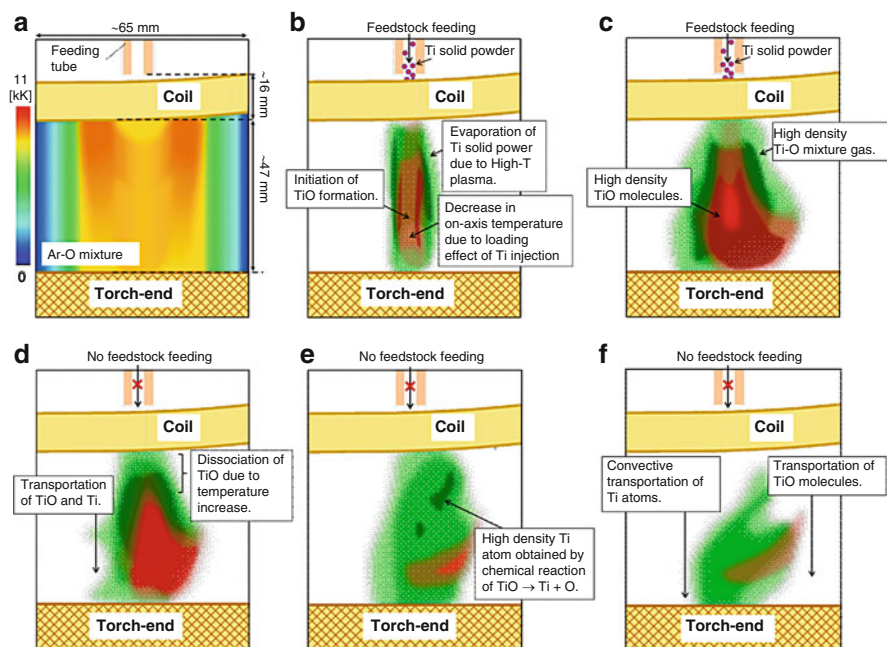


Fig. 18 Temporal and spatial variation of Ti atomic density and TiO molecular density in the ICTP torch estimated from two-dimensional spectroscopic observation results for 27%DF_{valve}: (a) Before feedstock injection into the ICTP torch ($t = 0$ ms); (b) Ti feedstock feeding, Ti evaporation, and TiO formation ($t \sim 7$ ms); (c) formation of high-density Ti–O mixture and TiO molecules ($t \sim 14$ ms); (d) TiO transport and TiO dissociation attributable to the increased temperature by stopping feedstock feeding ($t \sim 18$ ms); (e) formation of high-density Ti atoms attributable to dissociation reaction of $\text{TiO} \rightarrow \text{Ti} + \text{O}$ ($t \sim 20$ ms); and (f) convective transport of Ti atoms ($t \sim 22$ ms) (Kodama et al. 2016)

The feedstock feeding starts by opening the valve. The feedstock powder from the valve arrives at the tip of the water-cooled tube into the thermal plasma within 7–8 ms, as presented in Figs. 17c and 18b. The injected feedstock powder begins to evaporate very quickly in 0.5 ms to generate Ti atoms just under the outlet of the feeding tube because of high temperature of the ICTP around 5000 K. The feedstock evaporation offers dense Ti atoms. The generated Ti atoms are transported to the axial direction downstream by flow of the carrier gas. The Ti atoms are also diffused in the radial direction because of high gradient in Ti atomic density formed by feedstock evaporation. At the same time, the on-axis temperature decreased rapidly to 2000–5000 K because of the cool carrier gas flow and also by the feedstock evaporation shown in Fig. 18b. Therefore, the time variation is estimated in the temperature just under the tube as presented in Fig. 17d. Because of this temperature decrease to 2000–5000 K, Ti and O are associated to produce precursor TiO molecules around the on-axis region according to the calculated equilibrium composition. This formation reaction occurs almost simultaneously with Ti feedstock evaporation: within 0.5 ms. Therefore, high-density Ti atomic gas is present rather in the off-axis region although high-density TiO molecular gas is present around the on-axis region.

Increasing Ti atomic density between $t = 8$ –10 ms promotes the TiO molecule formation reaction, resulting in the high-density TiO molecules at $t = 8$ –10 ms, as presented in Fig. 17e. In $t = 10$ –16 ms, the time variation of Ti atomic and TiO molecular densities becomes almost steady because of the balance between feedstock evaporation and the diffusive transportation of Ti atoms and TiO molecules. Therefore, the spatial distributions of Ti atom and TiO molecule are obtainable as shown in Fig. 18c.

When the feedstock feeding and evaporation are finished, the temperature just under the outlet of the feeding tube recovers to higher values of 9000 K in the torch, as shown in Fig. 17d. In this case, TiO molecules are dissociated, leading to decreasing TiO molecular density, as shown in Fig. 18d. At the same time, Ti atomic density is maintained, although the TiO molecular density is decreased because Ti atoms are regenerated by a dissociation reaction of TiO molecules, as presented in Fig. 18e. These TiO and Ti are transported downstream of the plasma torch and then to the reaction chamber.

As described above, high-density Ti atoms are created in the off-axis region. High-density TiO are produced in the on-axis region inside the plasma torch. They are then transported to the reaction chamber by gas flow. Such high-density Ti atoms can produce Ti clusters by homogeneous nucleation. Then they can be oxidized to create TiO_x clusters, i.e., the nuclei of TiO_2 NPs. However, the high-density TiO can also become TiO_x clusters by homogeneous nucleation with association. These clusters can grow by inhomogeneous processes including chemical vapor deposition from Ti, O, and TiO in gas phase. Then, coagulation and agglomeration occur to form NPs in the reaction chamber.

The observation results provided fundamental information related to evaporation of the Ti feedstock and transport of Ti atoms, in addition to the subsequent formation

and transport processes of TiO. These data are expected to be useful to assess highly efficient nanoparticle synthesis using inductively coupled thermal plasmas.

3 Conclusions

This chapter is devoted to description of the fundamentals and basics of nanoparticle synthesis using thermal plasmas. As described, thermal plasma is an effective heat source, a powerful tool to evaporate raw material feedstock and then to cool the evaporated material for formation of nanoparticles as a high-temperature gradient source. The thermal plasma method offers great potential to contribute to the construction of future society.

4 Cross-References

- ▶ Analytical Methods in Heat Transfer
- ▶ Droplet Impact and Solidification in Plasma Spraying
- ▶ Electrohydrodynamically Augmented Internal Forced Convection
- ▶ Evaporative Heat Exchangers
- ▶ Full-Coverage Effusion Cooling in External Forced Convection: Sparse and Dense Hole Arrays
- ▶ Heat Transfer in Arc Welding
- ▶ Heat Transfer in DC and RF Plasma Torches
- ▶ Heat Transfer in Plasma Arc Cutting
- ▶ Heat Transfer in Rotating Flows
- ▶ Heat Transfer in Suspension Plasma Spraying
- ▶ Macroscopic Heat Conduction Formulation
- ▶ Numerical Methods for Conduction-type Phenomena
- ▶ Phase Change Materials
- ▶ Plasma Waste Destruction
- ▶ Plasma-Particle Heat Transfer
- ▶ Radiative Plasma Heat Transfer
- ▶ Radiative Properties of Gases
- ▶ Radiative Properties of Particles
- ▶ Radiative Transfer Equation and Solutions
- ▶ Single-Phase Convective Heat Transfer: Basic Equations and Solutions
- ▶ Single-phase Heat Exchangers
- ▶ Thermal Transport in Micro- and Nanoscale Systems
- ▶ Thermophysical Properties Measurement and Identification
- ▶ Turbulence Effects on Convective Heat Transfer
- ▶ Two-phase Heat Exchangers

References

- Ando Y, Zhao X, Hirahara K, Suenaga K, Bandow S, Iijima S (2000) Mass production of single-wall carbon nanotubes by the arc plasma jet method. *Chem Phys Lett* 323:580
- Anekawa Y, Koseki T, Yoshida T, Akashi K (1985) The co-condensation process of high temperature metallic vapors. *J Jpn Inst Metals* 49:451–456
- Araya T, Ibaraki Y, Endo Y, Hioki S, Kanamaru M (1988) Arc apparatus for producing ultrafine particles, US Patent 4732369
- Barolo G, Livraghi S, Chiesa M, Cristina M, Paganini C, Giamello E (2012) Mechanism of the photoactivity under visible light of N-doped titanium dioxide. Charge carries migration in irradiated N-TiO₂ investigated by electron paramagnetic resonance. *J Phys Chem C* 116:20887–20894
- Biju KP, Jain MK (2008) Effect of crystallization on humidity sensing properties of sol-gel derived nanocrystalline TiO₂ thin films. *Thin Solid Films* 516:2175–2180
- Bilodeau JF, Proulx P (1996) A mathematical model for ultrafine iron powder growth in thermal plasmas. *Aerosol Sci Technol* 24:175–189
- Bora B, Aomoa N, Bordoloi RK, Srivastava DN, Bhuyan H, Das AK, Kakati M (2012) Freeflowing, transparent γ -alumina nanoparticles synthesized using a supersonic thermal plasma expansion process. *Curr Appl Phys* 12(3):880–884
- Bora B, Aomoa N, Bordoloi RK, Srivastava DN, Bhuyan H, Das AK, Kakati M (2013) Studies on a supersonic thermal plasma expansion process for synthesis of titanium nitride nanoparticles. *Powder Technol* 246:413–418
- Bora B, Saikia BJ, Borgohain C, Kakati M, Das AK (2010) Numerical investigation of nanoparticle synthesis in supersonic thermal plasma expansion. *Vacuum* 85:283
- Boulos MI, Jurewicz J, Guo J (2006) Induction plasma synthesis of nanopowders. US Patent 8013269 B2
- Bystrzejewski M, Huczko A, Lange H, Plotczyk WW, Stankiewicz R, Pichler T, Gemming T, Rummeli MH (2008) A continuous synthesis of carbon nanotubes by dc thermal plasma jet. *Appl Phys A Mater Sci Process* 91:223
- Cheng Y, Tanaka M, Watanabe T, Choi SY, Shin MS, Lee KH (2014) Synthesis of Ni₂B nanoparticles by RF thermal plasma for fuel cell catalyst. *J Phys Conf Ser* 518:012026
- Choi SI, Nam JS, Kim JI, Hwang TH, Seo JH, Hong SH (2006) Continuous process of carbon nanotubes synthesis by decomposition of methane using an arc-jet plasma. *Thin Solid Films* 506–507:244
- Colombo V, Ghedini E, Gherardi M, Sanibondi P (2012) Modelling for the optimization of the reaction chamber in silicon nanoparticle synthesis by a radio-frequency induction thermal plasma. *Plasma Sources Sci Technol* 21(5):055007
- Colombo V, Ghedini E, Gherardi M, Sanibondi P (2013) Evaluation of precursor evaporation in Si nanoparticle synthesis by inductively coupled thermal plasmas. *Plasma Sources Sci Technol* 22(3):035010
- Crowe CT, Sharma MP, Stock DE (1977) The particle-source-in cell (PSI-cell) model for gas-droplet flows. *J Fluids Eng* 99:325–332
- Cruz ACD, Munz RJ (1997) Vapor phase synthesis of fine particles. *IEEE Trans Plasma Sci* 25:1008–1016
- Cruz ACD, Munz RJ (2001) Nucleation with simultaneous chemical reaction in the vapor-phase synthesis of AlN ultrafine powders. *Aerosol Sci Technol* 34:499–511
- Désilets M, Bilodeau JF, Proulx P (1997) Modelling of the reactive synthesis of ultrafine powders in a thermal plasma reactor. *J Phys D Appl Phys* 30:1951–1960
- Ebbensen TW, Ajayan PM (1992) Large-scale synthesis of carbon nanotubes. *Nature* 358:220
- Eguchi K, Ko IY, Sugawara T, Lee HJ, Yoshida T (1989) Process control for the formation of fine SiC powders in thermal plasma frame. *J Jpn Inst Metals* 53:1236–1241
- Fauchais P, Vardelle A, Denoirjean A (1997) Reactive thermal plasmas: ultrafine particle synthesis and coating deposition. *Surf Coat Technol* 97:66

- Friedlander SK (2000) *Smoke, dust and haze*. Oxford University Press, New York
- Fuchs NA (1964) *Mechanics of aerosols*. Pergamon, New York
- Fudoligh AM, Nogami H, Yagi J (1997) Prediction of generation rates in 'reactive arc plasma' ultrafine powder production process. *ISIJ Int* 37:641
- Girshick SL, Chiu CP (1990a) Kinetic nucleation theory: a new expression for the rate of homogeneous nucleation from an ideal supersaturated vapor. *J Chem Phys* 93:1273–1277
- Girshick SL, Chiu CP (1990b) Numerical study of MgO powder synthesis by thermal plasma. *Aerosol Sci Technol* 21:641–650
- Girshick SL, Chiu CP, McMurry PH (1988) Modeling particle formation and growth in a plasma synthesis reactor. *Plasma Chem Plasma Process* 8:145–157
- Girshick SL, Chiu CP, McMurry PH (1990) Time-dependent aerosol models and homogeneous nucleation rates. *Aerosol Sci Technol* 13:465–477
- Girshick SL, Chiu CP, Muno R, Wu CY, Yang L, Singh SK, McMurry PH (1993) Thermal plasma synthesis of ultrafine iron particles. *J Aerosol Sci* 24:367–382
- Gitzhofer F (1996) Induction plasma synthesis of ultrafine SiC. *Pure Appl Chem* 68:1113
- Goortani BM, Mendoza-Gonzalez NY, Proulx P (2006) Synthesis of SiO₂ nanoparticles in RF plasma reactors: effect of feed rate and quench gas injection. *Int J Chem React Eng* 4:A33
- Gratzel M (2001) Photoelectrochemical cells. *Nature* 414:338–344
- Guo JY, Gitzhofer F, Boulos MI (1995) Induction plasma synthesis of ultrafine SiC powders from silicon and CH₄. *J Mater Sci* 30:5589
- Harada T, Yoshida T, Koseki T, Akashi K (1985) Co-condensation process of high temperature metallic vapors. *J Jpn Inst Metals* 45:1138–1145
- Iijima S, Ichihashi T (1993) Single-shell carbon nanotubes of 1-nm diameter. *Nature* 363:603
- Ishigaki T, Li JG (2007) Synthesis of functional nanocrystallites through reactive thermal plasma processing. *Sci Technol Adv Mater* 8:617–623
- Ishigaki T, Oh SM, Li JG, Park DW (2005) Controlling the synthesis of TaC nanopowders by injecting liquid precursor into RF induction plasma. *Sci Technol Adv Mater* 6:111–118
- Kakati M, Bora B, Sarma S, Saikia BJ, Shripathi T, Deshpande U, Dubey A, Ghosh G, Das AK (2008) Synthesis of titanium oxide and titanium nitride nanoparticles with narrow size distribution by supersonic thermal plasma expansion. *Vacuum* 82:833
- Kim KH, Choi H, Han C (2017) Tungsten micropowder/copper nanoparticle core/shell-structured composite powder synthesized by inductively coupled thermal plasma process. *Metall Mater Trans A: Phys Metall Mater Sci* 48(1):439–445
- Kim TH, Choi S, Park DW (2013) Effects of NH₃ flow rate on the thermal plasma synthesis of AlN nanoparticles. *J Korean Phys Soc* 63(10):1864–1870
- Kim KS, Cota-Sanchez G, Kingston CT, Imris M, Simard B, Soucy G (2007) Large-scale production of single-walled carbon nanotubes by induction thermal plasma. *J Phys D Appl Phys* 40:2375
- Kim YM, Kim KH, Kim B, Choi H (2016) Size and morphology manipulation of nickel nanoparticle in inductively coupled thermal plasma synthesis. *J Alloys Comp* 658:824–831
- Kim KS, Moradian A, Mostaghimi J, Alinejad Y, Shahverdi A, Simard B, Soucy G (2009) Synthesis of single-walled carbon nanotubes by induction thermal plasma. *Nano Res* 2:800
- Kim KS, Seo JH, Nam JS, Ju WT, Hong SH (2005) Production of hydrogen and carbon black by methane decomposition using dc-rf hybrid thermal plasmas. *IEEE Trans Plasma Sci* 33(2):813
- Ko EH, Kim T-H, Choi S, Park D-W (2015) Synthesis of cubic boron nitride nanoparticles from boron oxide, melamine and NH₃ by non-transferred Ar-N₂ thermal plasma. *J Nanosci Nanotechnol* 15(11):8515–8520
- Kodama N, Tanaka Y, Kita K, Ishisaka Y, Uesugi Y, Ishijima T, Sueyasu S, Nakamura K (2016) Fundamental study of Ti feedstock evaporation and the precursor formation process in inductively coupled thermal plasmas during TiO₂ nanopowder synthesis. *J Phys D Appl Phys* 49(30):305501
- Kodama N, Tanaka Y, Kita K, Uesugi Y, Ishijima T, Watanabe S, Nakamura K (2014) A method for large-scale synthesis of Al-doped TiO₂ nanopowder using pulse-modulated induction thermal plasmas with time-controlled feedstock feeding. *J Phys D Appl Phys* 47:195304

- Kulkarni NV, Karmakar S, Banerjee I, Sahasrabudhe SN, Das AK, Bhoraskar SV (2009) Growth of nanoparticles of Al_2O_3 , AlN and iron oxide with different crystalline phases in a thermal plasma reactor. *Mater Res Bull* 9:203–213
- Lee HJ, Eguchi K, Yoshida T (1990) Preparation of ultrafine silicon nitride, and silicon nitride and silicon carbide mixed powders in a hybrid plasma. *J Am Ceram Soc* 73:3356–3362
- Lee JE, Oh SM, Park DW (2004) Synthesis of nano-sized Al doped TiO_2 powders using thermal plasma. *Thin Solid Films* 457:230–234
- Lee SH, Oh SM, Park DW (2007) Preparation of silver nanopowder by thermal plasma. *Mater Sci Eng C* 27:1286
- Leparoux M, Schreuders C, Shin JW, Siegmann S (2005) Induction plasma synthesis of carbide nanopowders. *Adv Eng Mater* 7:349
- Li JG, Ikeda M, Ye R, Moriyoshi Y, Ishigaki T (2007) Control of particle size and phase formation of TiO_2 nanoparticles synthesized in RF induction plasma. *J Phys D Appl Phys* 40:2348–2353
- Li YL, Ishigaki T (2004) Controlled one-step synthesis of nanocrystalline anatase and rutile TiO_2 powders by in-flight thermal plasma oxidation. *J Phys Chem B* 108(40):15536–15542
- Li J, Zhao X, Wei H, Gu ZZ, Lu Z (2008) Macroporous ordered titanium dioxide (TiO_2) inverse opal as a new label-free immunosensor. *Anal Chem Acta* 625:63–69
- Malato S, Blanco J, Alarcon DC, Maldonado MI, Fernandez-Ibanez P, Gernjak W (2007) Photocatalytic decontamination and disinfection of water with solar collectors. *Catal Today* 122:137–149
- Marion F, Munz RJ, Dolbec R, Xue S, Boulos M (2007) Effect of plasma power and precursor size distribution on alumina nanoparticles produced in an inductively coupled plasma (ICP) reactor. *J Thermal Spray Technol* 17:533–550
- McGraw R (1997) Description of aerosol dynamics by the quadrature method of moments. *Aerosol Sci Technol* 27:255–265
- Mendoza-Gonzalez NY, Goortani BM, Proulx P (2007a) Numerical simulation of silica nanoparticles production in an RF plasma reactor: effect of quench. *Mater Sci Eng C* 27:1265–1269
- Mendoza-Gonzalez NY, Morsli ME, Proulx P (2007b) Production of nanoparticles in thermal plasmas: a model including evaporation, nucleation, condensation and fractal aggregation. *J Thermal Spray Technol* 17:533–550
- Murphy AB (2004) Formation of titanium nanoparticles from a titanium tetrachloride plasma. *J Phys D Appl Phys* 37:2841–2847
- Oh SM, Ishigaki T (2004) Preparation of pure rutile and anatase TiO_2 nanopowders using RF thermal plasma. *Thin Solid Films* 457:186–191
- Oh SM, Park DW (1998) Preparation of AlN fine powder by thermal plasma processing. *Thin Solid Films* 316:189
- Ohno S, Uda M (1984) Generation rate of ultrafine metal particles in hydrogen plasma: metal reaction. *J Jpn Ins Metals* 48:640. (in Japanese)
- Ostrikov K, Murphy AB (2007) Plasma-aided nanofabrication: where is the cutting edge? *J Phys D Appl Phys* 40:2223–2241
- Proulx P, Bilodeau JF (1989) Particle coagulation, diffusion and thermophoresis in laminar tube flows. *J Aerosol Sci* 20:101–111
- Proulx P, Mostaghimi J, Boulos MI (1985) Plasma–particle interaction effects in induction plasma modeling under dense loading conditions. *Int J Heat Mass Transf* 28:1327–1336
- Proulx P, Mostaghimi J, Boulos MI (1987) Heating of powder in an r.f. inductively coupled plasma under dense loading conditions. *Plasma Chem Plasma Process* 7:29–52
- Seo JH, Hong BG (2012) Thermal plasma synthesis of nano-sized powders. *Nucl Eng Technol* 44:9–19
- Shi Z, Lian Y, Liao FH, Zhou X, Gu Z, Zhang Y, Iijima S, Li H, Yue KT, Zhang SL (2000) Large scale synthesis of single-wall carbon nanotubes by arc-discharge method. *J Phys Chem Solids* 61:1031
- Shigeta M, Murphy AB (2011) Thermal plasmas for nanofabrication. *J Phys D Appl Phys* 44:174025

- Shigeta M, Watanabe T (2007) Growth mechanism of silicon-based functional nanoparticles fabricated by inductively coupled thermal plasmas. *J Phys D Appl Phys* 40:2407–2419
- Shigeta M, Watanabe T (2008) Numerical investigation of cooling effect on platinum nanoparticle formation in an inductively coupled thermal plasma. *J Appl Phys* 103:074903
- Shigeta M, Watanabe T (2010) Growth mechanism of binary alloy nanopowders for thermal plasma synthesis. *J Appl Phys* 108:043306
- Smoluchowski M (1916) Drei Vortrage uber Diffusion, Brownsche Molekularbewegung und Koagulation von Kolloidteilchen. *Z Physik Z* 17(557–571):585–599
- Son S, Taheri M, Carpenter E, Harris VG, McHenry ME (2002) Synthesis of ferrite and nickel ferrite nanoparticles using radiofrequency thermal plasma torch. *J Appl Phys* 91:7589
- Sone H, Kageyama T, Tanaka M, Okamoto D, Watanabe T (2016) Induction thermal plasma synthesis of lithium oxide composite nanoparticles with a spinel structure. *Jpn J Appl Phys* 55 (7S2):07LE04
- Soucy G, Jurewicz JW, Boulos MI (1995) Parametric study of the plasma synthesis of ultrafine silicon nitride powders. *J Mater Sci* 30(8):2008–2018
- Stein M, Kruis FE (2015) Scale-up of metal nanoparticle production. *NSTI: Adv Mater Tech Connect Briefs* 1:203–206
- Stein M, Kruis FE (2016) Optimization of a transferred arc reactor for metal nanoparticle synthesis. *J Nanopart Res* 18(9):258
- Tanaka M, Kageyama T, Sone H, Yoshida S, Okamoto D, Watanabe T (2016) Synthesis of lithium metal oxide nanoparticles by induction thermal plasmas. *Nano* 6(4):60
- Tanaka Y, Nagumo T, Sakai H, Uesugi Y, Nakamura K (2010) Nanoparticle synthesis using high-powered pulse-modulated induction thermal plasma. *J Phys D Appl Phys* 43:265201
- Tanaka Y, Tsume T, Guo W, Uesugi Y, Ishijima T, Watanabe S, Nakamura K (2012) A large amount synthesis of nanopowder using modulated induction thermal plasmas synchronized with intermittent feeding of raw materials. *J Phys D: Conf Ser* 406:012001
- Tanaka M, Watanabe T (2008) Vaporization mechanism from Sn-Ag mixture by Ar-H₂ arc for nanoparticle preparation. *Thin Solid Films* 516(19):6645–6649
- Thompson D, Leparoux M, Jaeggi C, Buha J, Pui DYH, Wang J (2013) Aerosol emission monitoring in the production of silicon carbide nanoparticles by induction plasma synthesis. *J Nanopart Res* 15:12
- Tong L, Reddy RG (2005) Synthesis of titanium carbide nano-powders by thermal plasma. *Scr Mater* 52:1253
- Tong L, Reddy RG (2006) Thermal plasma synthesis of SiC nano-powders/nano-fibers. *Mater Res Bull* 41:2303–2310
- Tsai YC, Hsi CH, Bai H, Fan SK, Sun DH (2012) Single-step synthesis of Al-doped TiO₂ nanoparticles using non-transferred thermal plasma torch. *Jpn J Appl Phys* 51:01AL01
- Uda M, Ohno S, Hoshi T (1983) Process for producing fine metal particles. *US Patent* 4376740
- Uda M, Ohno S, Okuyama H (1987) Process for producing particles of ceramic. *US Patent* 4642207
- Wang XH, Li JG, Kamiyama H, Katada M, Ohashi N, Moriyoshi Y, Ishigaki T (2005) Pyrogenic iron (III)-doped TiO₂ nanopowders synthesized in RF thermal plasma: phase formation, defect structure, band gap, and magnetic properties. *J Am Chem Soc* 127:10982–10990
- Watanabe T, Itoh H, Ishii Y (2001) Preparation of ultrafine particles of silicon base intermetallic compound by arc plasma method. *Thin Solid Films* 390(1–2):44–50
- Watanabe T, Tanaka M, Shimizu T, Liang F (2013) Metal nanoparticle production by anode jet of argon-hydrogen dc arc. *Adv Mater Res* 628:11–14
- Yoshida T, Akashi K (1981) Preparation of ultrafine iron particles using an RF plasma. *Trans Jpn Inst Metals* 22:371–378
- Yoshida T, Kawasaki A, Nakagawa K, Akashi K (1979) The synthesis of ultrafine titanium nitride in an rf plasma. *J Mater Sci* 14:1624–1630
- Yoshida T, Tani T, Nishimura H, Akashi K (1983) Characterization of a hybrid plasma and its application to a chemical synthesis. *J Appl Phys* 54:640–646

- Zhang C, Li JG, Uchikoshi T, Watanabe T, Ishigaki T (2010) (Eu³⁺-Nb⁵⁺)-codoped TiO₂ nanopowders synthesized via Ar/O₂ radio-frequency thermal plasma oxidation processing: phase composition and photoluminescence properties through energy transfer. *Thin Solid Films* 518:3531–3334
- Zhang C, Uchikoshi T, Li JG, Watanabe T, Ishigaki T (2014) Photocatalytic activities of europium (III) and niobium (V) co-doped TiO₂ nanopowders synthesized in Ar/O₂ radio-frequency thermal plasmas. *J Alloys Compd* 606:37–43